NASA/TP—2020-220002

Space Radiation and Impact on Instrumentation Technologies

John D. Wrbanek and Susan Y. Wrbanek
Glenn Research Center, Cleveland, Ohio

January 2020

NASA STI Program . . . in Profile

Since its founding, NASA has been dedicated to the advancement of aeronautics and space science. The NASA Scientific and Technical Information (STI) Program plays a key part in helping NASA maintain this important role.

The NASA STI Program operates under the auspices of the Agency Chief Information Officer. It collects, organizes, provides for archiving, and disseminates NASA's STI. The NASA STI Program provides access to the NASA Technical Report Server—Registered (NTRS Reg) and NASA Technical Report Server—Public (NTRS) thus providing one of the largest collections of aeronautical and space science STI in the world. Results are published in both non-NASA channels and by NASA in the NASA STI Report Series, which includes the following report types:

- TECHNICAL PUBLICATION. Reports of completed research or a major significant phase of research that present the results of NASA programs and include extensive data or theoretical analysis. Includes compilations of significant scientific and technical data and information deemed to be of continuing reference value. NASA counter-part of peer-reviewed formal professional papers, but has less stringent limitations on manuscript length and extent of graphic presentations.

- TECHNICAL MEMORANDUM. Scientific and technical findings that are preliminary or of specialized interest, e.g., "quick-release" reports, working papers, and bibliographies that contain minimal annotation. Does not contain extensive analysis.

- CONTRACTOR REPORT. Scientific and technical findings by NASA-sponsored contractors and grantees.

- CONFERENCE PUBLICATION. Collected papers from scientific and technical conferences, symposia, seminars, or other meetings sponsored or co-sponsored by NASA.

- SPECIAL PUBLICATION. Scientific, technical, or historical information from NASA programs, projects, and missions, often concerned with subjects having substantial public interest.

- TECHNICAL TRANSLATION. English-language translations of foreign scientific and technical material pertinent to NASA's mission.

For more information about the NASA STI program, see the following:

- Access the NASA STI program home page at http://www.sti.nasa.gov

- E-mail your question to help@sti.nasa.gov

- Fax your question to the NASA STI Information Desk at 757-864-6500

- Telephone the NASA STI Information Desk at 757-864-9658

- Write to:
  NASA STI Program
  Mail Stop 148
  NASA Langley Research Center
  Hampton, VA 23681-2199

NASA/TP—2020-220002

Space Radiation and Impact on Instrumentation Technologies

John D. Wrbanek and Susan Y. Wrbanek
Glenn Research Center, Cleveland, Ohio

National Aeronautics and
Space Administration

Glenn Research Center
Cleveland, Ohio 44135

January 2020

Acknowledgments

This work was sponsored by the NASA Glenn Research Center Space Technology Projects Office, Space Science Projects Office, and Innovation and Integration Office. The authors wish to thank members of the SPAGHETI collaboration team for their technical contributions and support: Gustave Fralick (Glenn), Pamela Clark (NASA Jet Propulsion Laboratory), Nathan Schwadron (University of New Hampshire), Benjamin Malphrus (Morehead State University), Roger McNeil (Morehead State University), Michael Collier (NASA Goddard Space Flight Center), J. Bern Blake (The Aerospace Corporation), and William Crain (The Aerospace Corporation). The technical support at Glenn, including Elizabeth McQuaid (Glenn), Nicholas Varaljay (Glenn), Wentworth Trevor John (HX5-Sierra LLC), Charles Blaha (Jacobs Technology), José Gonzalez (HX5-Sierra LLC), and many others are sincerely appreciated. We also thank Dale Force (Glenn) and Fred Elliot (Glenn) for their reviews and comments.

This report is a formal draft or working paper, intended to solicit comments and ideas from a technical peer group.

This report contains preliminary findings, subject to revision as analysis proceeds.

Level of Review: This material has been technically reviewed by technical management.

Available from

NASA STI Program
Mail Stop 148
NASA Langley Research Center
Hampton, VA 23681-2199

National Technical Information Service
5285 Port Royal Road
Springfield, VA 22161
703-605-6000

This report is available in electronic form at http://www.sti.nasa.gov/ and http://ntrs.nasa.gov/

Contents

Space Radiation and Impact on Instrumentation Technologies

John Wrbanek and Susan Wrbanek
National Aeronautics and Space Administration
Glenn Research Center
Cleveland, Ohio 44135

Summary

Understanding the interactions of the Sun, Earth, and other natural and man-made objects in the solar system with the space radiation environment is crucial for improving activities of humans on Earth and in space. An important component of understanding these interactions is their effects on the instrumentation required in the exploration of air and space. NASA Glenn Research Center fills the role of developing supporting technologies to enable improved instruments for space science missions as well as for aeronautics and ground-based applications. In this review, the space radiation environment and its effects are outlined, as well as the impact it has on instrumentation and the technology that Glenn is developing to improve performance for space science.

1.0 Introduction

In very general terms, space radiation is created when matter is ejected from stars, stripped down to individual atoms and electrons, and accelerated to near light speed around stellar systems millions of light years away as well as by our own solar system. This radiation along with the gamma rays and neutral particles created in collisions in interstellar and interplanetary space have characteristics that vary for different regions of space, as does its impact on man-made and natural objects.

A little over a decade from the discovery of naturally occurring background radiation in 1900, indications were seen that a significant portion of this ionizing background was coming from extraterrestrial sources. In the late 1940s and early 1950s, these "cosmic rays" were the source of high-energy-particle physics research before the advent of large particle accelerators. The discovery of the more common subatomic particles—muons, pions, kaons, and lambda baryons—as well as discovery of important particle properties (such as quark flavors, charge conjugation parity symmetry (CP) violation, and neutrino mass) owe their discovery to cosmic ray experiments (De Angelis, 2013). At present, the study of space radiation is still very important for astrophysics and particle physics. Fermi Gamma-ray Space Telescope (FGST), Alpha Magnetic Spectrometer (AMS), and Sudbury Neutrino Observatory (SNO) (Boger et al., 2000; Lechanoine-Leluc et al., 2005; Morselli et al., 2008) are examples of recent astrophysics and particle physics experiments reliant on cosmic rays.

In this review of space radiation and its impact on instrumentation technologies, we will discuss the radiation environment as space science, the variety of space radiation environments, radiation effects, radiation risks to space science instrumentation technologies, and space radiation detector development, followed by concluding remarks. Symbols and acronyms used in this report are found in the Appendix.

2.0 The Radiation Environment as Space Science

Naturally occurring space radiation is always with us. It occurs when atoms, ions, or subatomic particles are accelerated to high velocity by processes such as solar particle events (SPEs) and coronal mass ejections (CMEs) from the Sun or stars creating solar energetic particles (SEPs), the solar wind, trapped radiation in magnetic field "belts," and galactic cosmic rays (GCRs) from outside our solar system (as shown in Figure 1). Space radiation can take the form of fast-moving atoms, subatomic particles, ions, or high-energy electromagnetic waves. Anywhere that matter exists, there is a potential to have energetic charged and/or neutral particles. Anywhere that changing electromagnetic fields exist, or electromagnetic fields interacting with moving charges, the potential for both particle and electromagnetic-wave radiation exists.

To answer compelling science questions and to provide crucial knowledge that enables robotic space missions or crewed spaceflights, the space radiation environment is a subject of ongoing study in a variety of space science fields.

2.1 Heliophysics

Heliophysics is the study of our Sun, its heliosphere (the exotic outer atmosphere of the Sun formed by the solar wind), and its interaction with planetary bodies and interstellar space. The understanding and modeling of the transport and interaction of space radiation in this environment affects mission planning and operation for both crewed and uncrewed missions. For example, one research area is the attempt to gain an understanding of how solar activity is anticorrelated with

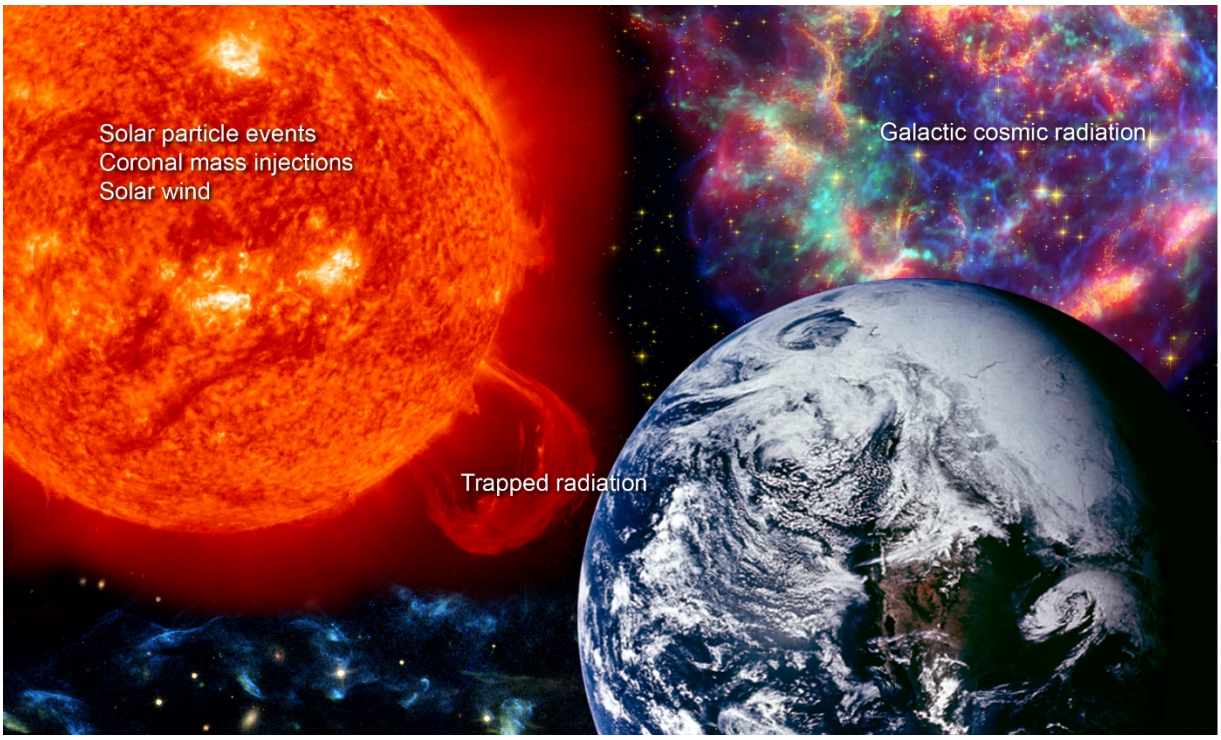

Figure 1.—Sources of space radiation.

GCR flux in the heliosphere. There are fewer GCR ions observed in the solar system when there appears to be more solar activity (Beer, Vonmoos, and Muscheler, 2006).

Another topic area of research is the study of observed magnetic field variations in the interplanetary medium down to the submillihertz scale. These variations are believed to result from transient structures in the heliospheric plasma. These transients result in an anisotropy in SEPs and GCR fluxes, and understanding these mechanisms will further clarify the transport mechanisms of ions in the heliosphere (Gosling, 2007; Mulligan et al., 2008)

2.2 Astrophysics

All stars are believed to have their own heliospheres, each interacting with the interstellar medium as well as the GCR flux. One area of study is the interactions of GCR ions in the interstellar medium. These interactions form a flux of lighter ions in a process referred to as "Cosmic Ray Spallation." Understanding the observed abundances of the extrasolar lighter heavy ions of atomic number $2 < Z < 6$ will allow a better understanding of the propagation and diffusion properties of the interstellar medium (Aguilar et al. 2010; Strong and Moskalenko, 1998; Vangioni-Flam, Casse, and Audouze, 2000).

There are also anomalous cosmic rays (ACRs) that originate as neutral atoms in the interstellar gas but are ionized by interactions with the Sun's heliosphere. The composition of ACRs is different from solar wind and GCRs in both energy and ion types. Observations of these ACRs can provide a more detailed understanding of the composition of the interstellar medium (Mewaldt, 1996).

2.3 Lunar and Planetary Science

The impact of SEP and GCR ions on the surfaces of planetary bodies produces albedo particles. An incoming ion fragments the target nucleus into lighter nuclei and subatomic particles. Heavier target ions also involve nuclear excitation and hadronic cascades. The distribution of the cascading albedo particles is dependent on the distribution of the incoming particles. For proton interactions involving hydrogen, the interactions should be simple knock-on collisions producing albedo protons and neutrons of higher energy than of those produced from heavier ion collisions. Understanding the particle flux and energy distributions from lunar and planetary surfaces can then give an understanding of composition (Wilson et al., 2012; Wilson et al., 2013).

2.4 Human Health and Spaceflight

Studies have noted that correlation exists between GCRs and geomagnetic activity among natural biological phenomena, including cell killing, mutation, aberration, carcinogenesis, heart rate variability, arrhythmias, heart attack, sudden cardiac death (SCD), and incidences of giant cell arteritis and

rheumatoid arthritis (Singh, Siingh, and Singh, 2011; Cornélissen et al., 2002; Stoupel, 2006; Stoupel et al., 2006; Wing et al., 2015). Additionally, cosmic radiation has been linked to software electrical resets in implantable cardioverter defibrillators during air travel. Data from research performed by S. Dimitrova in 2001 and 2002 indicates relationships to geomagnetic activity of systolic blood pressure, diastolic blood pressure, arterial blood pressure, pulse pressure, heart rate, and subjective psychophysiological complaints (Dimitrova, 2006).

Additionally, a recent study by Vipan K. Parihar et al. reports studies were undertaken to test for central nervous system damage from radiation that is expected to be encountered by people traveling to Mars. Rats were exposed to energetic charged particles of oxygen and titanium to simulate 5- and 30-cGy doses of radiation. Evidence for several types of damage to the central nervous system were observed. Evidence for long-term cognitive dysfunction was observed in the inability of radiated test animals to distinguish a novel object from a familiar object, and there was evidence of impaired memory. Damage to neurons was evident in animals studied and included reduced complexity, reduced spine density, and reduction of some spine types in neurons of the prefrontal cortex (Parihar et al., 2016). The prefrontal cortex, located in the frontal lobe of the mammalian brain is thought to be used for planning complex cognitive behavior, decision making, expression of personality, and moderation of social behavior (Miller, Freedman, and Wallis, 2002).

Additionally, reductions in the branching complexity of neurons in the prefrontal cortex were observed following exposure to the radiation and was correlated with changes in the individual behavioral performance. Radiation similar to cosmic rays was also observed to induce neuroinflammation. A concern that arose from this study was that much of the damage induced by cosmic radiation to the central nervous system showed no signs of repair in the test rodents 6 months following the radiation exposure (Parihar et al., 2016).

2.5 Earth Science

The extraterrestrial radiation environment interacts with the atmosphere in complex ways. Showers of cosmic ray particles can initiate a runaway breakdown of an electric field in a thundercloud, triggering lightning, and additionally lightning can generate x-ray and gamma-ray emissions (Gurevich and Milikh, 1999). Over the years, several studies have indicated that the amount of cloud cover on Earth is linked to the bombardment by GCRs.

2.5.1 Cloud Cover

Although cloud cover and precipitation depends on seasonal cycles, ocean temperature cycles, and possibly other effects on the atmosphere, many studies have linked solar activity to clouds on Earth. In 2016, Svensmark et al. published the results of a detailed study of the solar influence on clouds on the Earth. They found a greater than 95 percent correlation between Forbush decreases (or Forbush events, which are sudden minimizations of GCR activity following a CME), and a decrease in cloud fraction (Svensmark et al., 2016). Changes in the concentration of low cloud cover consistent with variation in cosmic ray flux have been noted in a variety of studies (Marsh and Svensmark, 2000; Kniveton, 2004; Perry, 2007).

A study performed in England found a small, but notable effect of cosmic rays on clouds. Diffuse fraction (diffuse light due to cloud cover) increased with an increase in neutron arrival on the Earth. Neutron arrival appears to increase with increased GCR arrival (Harrison and Stephenson, 2006). Pudovkin and Veretenensko (1995) studied correlations of local noon cloud cover data and GCR flux at several stations in Russia. Their data strongly suggest that changes in cloud cover are linked to changes in the flux of cosmic ray particles having energies from several hundred to approximately 1,000 MeV. They found that the strongest correlation was in the decrease of clouds 1 or 2 days following a Forbush decrease at latitudes between 60° and 64° N. They noted stronger amplitude to the correlation in the winter, though a correlation was still observed for summer months. In this study, high-level cirrus clouds appear to have been most affected.

In addition, a study performed in Germany of clouds at various heights showed that an additional, though weak, effect of GCRs on high clouds and aerosols is real (Rohs et al., 2010). Even short-term changes of timeframes, which range from 6 hours to 3 months, in cloud cover have been found in both the northern and southern hemispheres that appear to correlate with galactic cosmic ray flux (Brown, 2008). Pallé, Butler, and O'Brien (2004) investigated to see if correlation of low cloud cover and cosmic ray flux appeared to be regional. They found stronger correlation in the midlatitudes of 40° to 60°, both north and south. They found that correlations with location and latitude appeared to change and be more or less noticeable over time. A latitude-dependent and location correlation phenomenon seems to have also been noted by Rohs et al. (2010) in a study of high-level clouds.

2.5.2 Lightning

Studies of the relationship of charged particles from solar processes or deep space to lightning are still in the early stages of scientific inquiry. Much about the relationship between space radiation and planetary atmospheric phenomena remains to be understood.

A study performed by members of the Department of Meteorology at the University of Reading found that increases in lightning rates followed the arrival of fast solar wind streams

at the Earth (Scott et al., 2014). An earlier 8-year study using different lightning detection networks based in Germany and Austria covering different areas of middle Europe yielded some apparent correlation with solar activity with one lightning monitor, but not another (Schlegel et al., 2001). However, the account of that research does mention that the Alps run between the two monitored areas that were studied, but the study did not include any factors due to geographic influence.

A further investigation into possible links between lightning and cosmic ray flux over the United States between latitudes 25° and 45° N for the period from 1990 to 2005 was performed by Chronis (2009). The data studied appear to show a 4- to 5-day window of time between a Forbush decrease and minimization of lightning activity. A 2014 study of lightning over the United Kingdom indicates a difference in lightning and thunder rates depending on the relative direction of the Sun's magnetic field relative to the Earth's magnetic field (Owens et al., 2014). The study showed an increase of 40 to 60 percent more thunderstorm activity that could not be explained by seasonal variation when the polarity of the heliospheric magnetic field pointed toward the Sun.

A.V. Gurevich and colleagues (Gurevich, Zybin, and Roussel-Dupre, 1999; Gurevich, and Zybin, 2001; Gurveich and Zybin, 2005) found that the conventional explanation of lightning formation in many textbooks was inadequate to describe the entire phenomenon: from the onset of lightning to the radio, gamma-ray, and x-ray emissions associated with lightning. Their analysis showed that there is an insufficient number of thermally generated high-energy electrons to trigger lightning. Rather, they developed a model explaining that cosmic rays ionize air molecules, thus "seeding" the atmosphere with high-energy free electrons. Secondary fast electrons released by the energy of the ions created by the cosmic rays ionize other air molecules in an electric field. This process also generates a sufficient number of slow electrons for an eventual runaway breakdown of the air. They use the term "runaway breakdown" to describe the process by which cosmic rays trigger lightning. This runaway breakdown also generates additional x-ray and gamma-ray flashes inside thunderstorms (Gurevich and Milikh, 1999).

Cosmic rays not only generate free electrons that trigger lightning, but lightning also produces its own ionizing radiation. There are radio events both before and after lightning. Additionally, thunderclouds have been found to have "intense x-ray bursts both inside and beneath" (Milikh and Roussel-Dupré 2010). The x-ray energies have been measured to be "around 50keV…and are well correlated with lightning events" (Milikh and Roussel-Dupré, 2010). Gamma-ray emission with energies ranging from 2 to 10 MeV also accompanies lightning. Moore et al. (2001) recorded gamma radiation bursts greater than 1 MeV in a 1 to 2 ms time interval before cloud-to-ground negative lightning strikes during experiments at South Baldy Peak in New Mexico. The bursts they recorded continued until the first return stroke began.

Additionally, atmospheric electric fields have an effect on the acceleration of charged particles. Temporal fluctuations in cosmic rays have been attributed to large fluctuations of atmospheric electric fields during thunderstorms. Dorman et al. (2003) have found that the atmospheric field in thunderstorms influences both positive and negative muons, electrons, positrons, and the temporal variation of cosmic rays.

3.0 Variety of Space Radiation Environments

The local space radiation environment created by the interaction of cosmic rays with the planetary surfaces, atmospheres, and magnetic fields is dependent on the physical environment, producing a variety of effects.

3.1 Cosmic Rays in Terrestrial Environments

The form of space radiation with the broadest impact as seen on Earth are the generic "cosmic" rays detected from the ground up to the lower troposphere at elevations less than 5.5 km (18,000 ft). These "rays" are mostly subatomic particles, primarily muons and neutrinos produced by interactions of incoming protons in the air. Figure 2 shows the mechanisms of the major components of atmospheric cosmic rays:

$K^{\pm,0}$	kaons
$\lambda^{\pm,0}$	lambda baryons
$\pi^{0,\pm}$	pions
p	protons
n	neutrons
ν_e, $\overline{\nu}_e$	electron neutrinos
ν_μ, $\overline{\nu}_\mu$	muon neutrinos
$\mu^{\pm}$	muons
e^{+}	positrons
e^{-}	electrons
γ	gamma rays

Muons ($\mu^{\pm}$) and neutrinos (ν, $\overline{\nu}$) are the decay products of short-lived pions ($\pi^{\pm}$), and muons decay into electrons (e^{-}), positrons (e^{+}), and more neutrinos. Neutrinos interact very weakly; however, muons are ionizing with an observed energy peak at 3 GeV at sea level and an intensity of $1/cm^2 \cdot min$ (Olive et al., 2014).

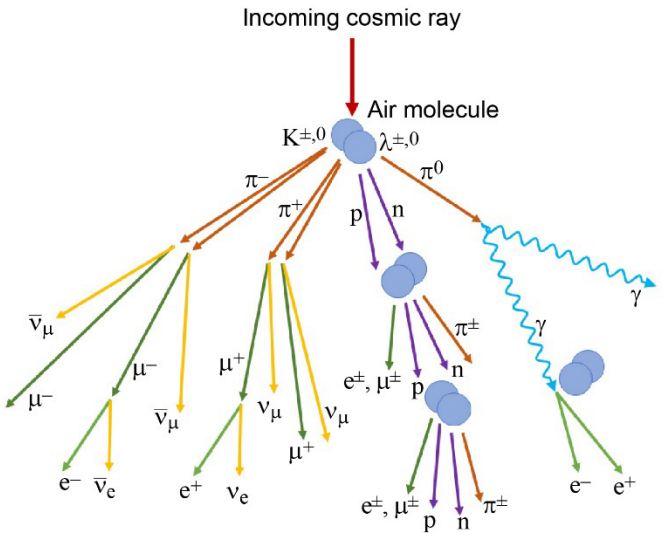

Figure 2.—Mechanisms of primary components of atmospheric cosmic rays (based in part on Bowersox (2011)).

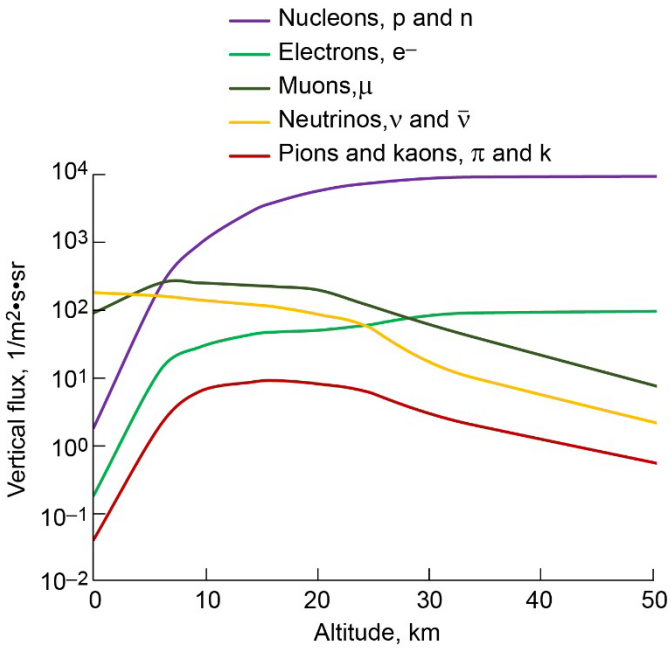

Figure 3.—Vertical fluxes of cosmic rays in atmosphere, derived from measurements of cosmic ray particle energies > 1 GeV (based on Olive et al., 2015).

The next prevalent flux is that of protons and neutrons (nucleons p and n, respectively), remnants of the incoming protons and neutrons from the outer atmosphere. Also seen are electrons, positrons, and photons (gamma rays (γ) and x-rays) that are generally products of cascades from the decay of muons, pions, kaons (K), and lambda baryons (λ) produced by the interaction of cosmic-ray nucleons with air.

In the upper troposphere and stratosphere, the nucleon flux is the more dominant source of observed cosmic radiation. The incoming flux comprises primarily relativistic protons with approximately 10 percent neutrons from the outer atmospheric regions. At about an altitude of 15 km (50,000 ft), the incoming protons have traversed the density-normalized attenuation length of 121 g/cm^2 in air from outer space, resulting in a peak intensity of secondary radiation. As the nucleon flux drops exponentially through the atmosphere, so does the secondary flux—with the exception of muons, which are longer lived than other secondary particles. The variation of vertical flux of major atmospheric cosmic ray components with atmosphere and altitude is shown in Figure 3.

3.2 Low Earth Orbit and Upper Atmosphere

In low Earth orbit (LEO) from 160 to 2,000 km altitude, the radiation environment is composed primarily of the space radiation not deflected by Earth's magnetic field. The peak energy of the ions in LEO was measured by the AMS–1 instrument on the International Space Station (ISS) to be approximately 20 GeV/u, and a secondary proton spectrum was seen from <1 to 6 GeV (depending on latitude). The secondary spectrum was found to be due to ions escaping from the radiation belts peaking at <10 MeV (Alcaraz et al., 2000b). Based on the measured linear energy transfer (LET), this secondary spectra appears to be limited to >1.40-MeV/u ions (Badhwar, 2001).

High-energy electrons and positrons created by distant supernova and accretion disks also trickle through the Earth's magnetic field. The LEO e^- and e^+ fluxes were also measured by AMS–1 (Alcaraz et al. 2000a), with electrons peaking at 500 MeV and positrons at 4 GeV. As with the ions, a secondary flux of escaped leptons from the radiation belts is seen in LEO to be <1 GeV, also varying with latitude.

3.3 Radiation Belts (Trapped Ions and Electrons)

Proceeding to middle Earth orbit (MEO, the region from 2,000 to 35,786 km altitude), the radiation field is dominated by the charged particles trapped by the Earth's magnetic field. The magnetic field of the Earth is formed by a spinning molten iron core that acts as a large magnet, the magnetic field of which deflects charged particles near the Earth. Interaction of the magnetic field with the ambient interplanetary medium forms a magnetosphere (Tribble ,2003; Russell, 1993).

The structure of the magnetosphere is outlined in Figure 4. The magnetosphere consists of a (1) bow shock, where the solar wind (the stream of protons from the Sun) is slowed; (2) the magnetosheath behind the bow shock that contains thermalized

solar plasma; (3) the magnetopause, where the thermalized solar plasma pressure is balanced by the plasma pressure generated by the magnetosphere; (4) the magnetotail, where the magnetic field is stretched out by the solar wind behind the dipole; and (5) the plasmasphere, where plasma is trapped by the magnetic field. The radiation belts are formed in the plasmasphere of the Earth's magnetosphere.

There are two distinct radiation belts in the plasmasphere named the "Van Allen belts," after their discoverer. There is an inner belt between 3,200 and 16,000 km in altitude (1.5 and 3.5 Earth radii (R_E) from Earth's center), and an outer belt 13,000 to 38,000 km altitude (3 to 7 R_E), which can extend out to 57,000 km (10 R_E). The electron and proton distributions in these belts are shown in Figure 5. These are very rough dimensions since the belts are defined by the interactions between the solar wind and the magnetic field; therefore, the Van Allen belts' distributions will fluctuate with solar activity. Geosynchronous Earth orbit (GEO) at a 35,786 km altitude is in the outer reaches of the outer belt, as are the retrograde high Earth orbits (HEOs) beyond GEO. Lunar orbit at about 384,000 km from Earth's center puts each full Moon within the magnetotail, which extends out to nearly 20 times that distance. Outside of the magnetotail, the radiation environment beyond 10 R_E from the center of the Earth (57,000 km altitude) is that of deep space.

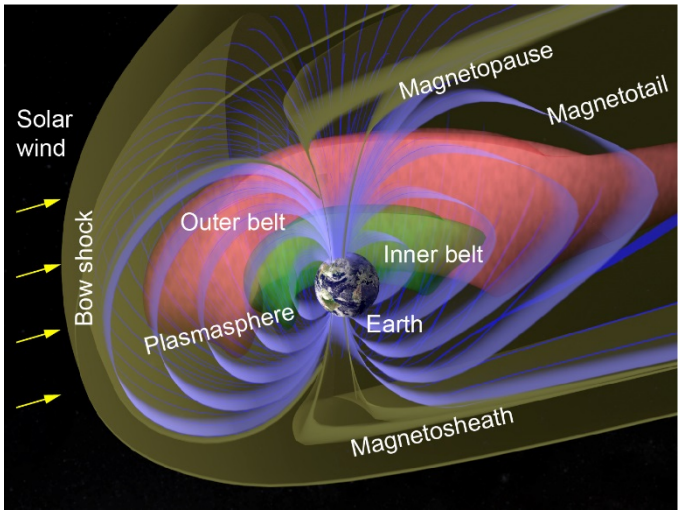

Figure 4.—Structure of Earth magnetosphere with magnetopotentials in blue, inner radiation belt in green, and outer radiation belt in red.

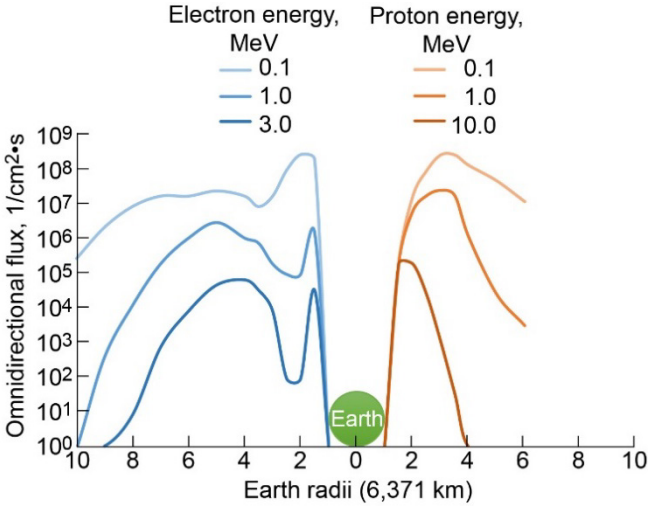

Figure 5.—Electron and proton spectra of Van Allen trapped radiation belts (based on Tribble (1993)).

3.4 Planetary Interactions

All planets have a version of a magnetosphere interacting with the solar wind, but only Mercury, Earth, Jupiter, Saturn, Uranus, and Neptune have magnetospheres defined by the planets' magnetic cores, referred to as "intrinsic magnetospheres." Other planets, moons, asteroids, and comets have magnetospheres defined through the ionization of their atmosphere or surface material by solar radiation; that is, "induced magnetospheres."

3.4.1 Venus and Mars

Venus may lack a magnetic field, but its proximity to the Sun and the presence of a thick atmosphere as a source of ions induces a magnetosphere similar to that in Figure 4, but without the magnetic field. A bow shock, magnetosheath, magnetopause, and magnetotail are formed by the current of the solar wind streaming around the planet. Measurements of the induced magnetic field around Venus by the Venus Express spacecraft suggests that the solar wind is completely deflected around the planet so that only radiation entering the atmosphere are GCR ions (Zhang et al., 2007).

With an atmospheric density of 67 kg/m³ on the surface, any proton flux that would reach the surface of Venus is considerably attenuated. The density-normalized attenuation length of a cosmic ray shower in Venus' carbon dioxide atmosphere is 118 g/cm²—very similar to that of Earth's atmosphere, but at nearly 55 times the density. Thus, the attenuation length at the surface of Venus is 17.6 m, such that the incoming cosmic radiation flux is expected to be completely attenuated and considered nonionizing at the surface.

At 1.52 AU from the Sun, Mars experiences less solar wind with increased GCR flux. The tenuous atmosphere shifts the energy of incoming ions lower to 50 MeV/u. Like Venus, Mars' carbon dioxide atmosphere has a density-normalized

attenuation length of 118 g/cm², but with a mean surface pressure of 600 Pa (0.087 psi), this length is 2,500 km, well beyond the 200-km thickness of its atmosphere. Albedo particle flux generated by incoming ions are primarily in the form neutrons from the surface (Clowdsly et al., 2005).

3.4.2 Jupiter and Outer Planets

Jupiter's magnetosphere fills a volume that is a million times the volume of Earth's, and it has a magnetotail that stretches 5 AU downstream of the solar wind. The magnetosphere is very dynamic, not only because of its size, but also because of the rotational speed of the planet's core, which accelerates trapped particles. The Galilean moons have their own induced magnetospheres produced by both photoionization from the Sun and from sputtering of their surfaces by the Jovian magnetosphere. The closest moon Io is subject to severe tidal heating, causing violent volcanic activity, which results in a tenuous atmosphere that is also sputtered away by the magnetosphere. These ions and electrons add to the particles trapped in Jupiter's radiation belts, with the resulting densities modeled as shown in Figure 6 (Garrett, 2008). Thus, the trapped radiation in the Jupiter ion and electron radiation belts is 60 times that found in Earth's radiation belts (Russell, 1993; Paranicas et al., 2009).

The other outer planets have magnetic fields weaker than Jupiter. Because of its size, Saturn's largest moon Titan enhances the magnetosphere of Saturn through solar ionization of its thick atmosphere, having its own bow shock and tail as it moves through the trapped particles of Saturn's radiation belts. With still-weaker magnetic fields, the magnetospheres of Uranus and Neptune are less dynamic and see less enhancement by their large major moons (Russell, 1993).

3.4.3 Asteroid and Planetary Surfaces

On objects without atmospheres such as small moons, asteroids, distant comets, and spacecraft, the radiation field also has a component that comprises energetic particles emitted by the surface of the objects on which the radiation from outer space impinges. This albedo radiation from surfaces of rocky objects or spacecraft is formed by direct interaction of space radiation with exposed material. For high-energy interactions, ionization results in photon emission and cascades of electrons and positrons from the airless surface. Direct collisions of ions with nuclei result in nuclear spallation, or the fragmentation of the nuclei into a shower of high-energy protons, neutrons, electrons, and gamma rays. The combination of these effects gives the radiation environment on an exposed surface a different composition than in deep space. Table I shows the relative source percentages of dose modeled for Lunar Reconnaissance Orbiter (LRO) orbit (altitude between 20 and 165 km from the lunar surface) around the Moon (Spence et al., 2013).

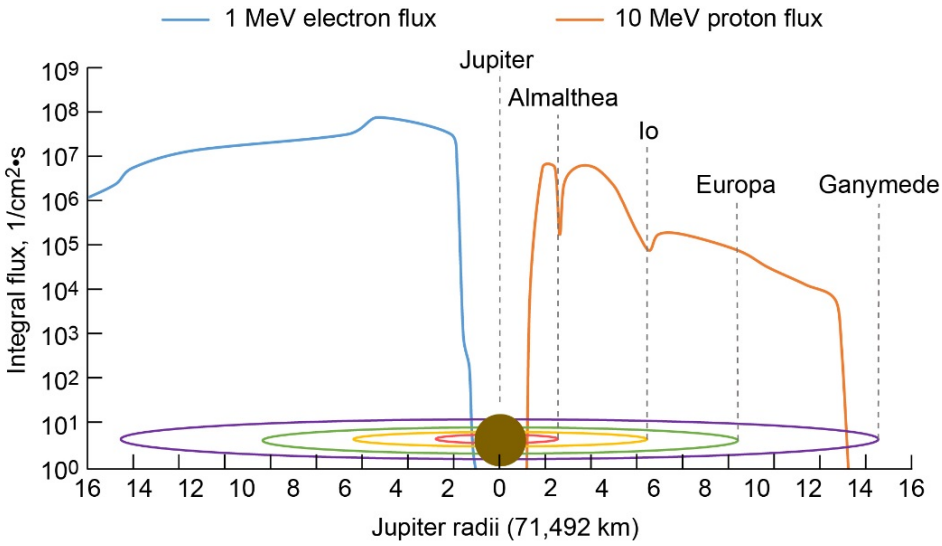

Figure 6.—Modeled 1-MeV electron and 10-MeV proton integral equatorial fluxes for Jovian magnetosphere radiation belts, with larger moon orbits labeled (based on Garrett (2008)).

3.5 Deep Space (GCR and Solar)

The most basic radiation environment for space science is that of deep space, specifically in the heliosphere of the solar system outside of the influence of planetary magnetospheres. The components of deep space radiation are outlined in Table II. The ever-present GCR background comprises ions that originate outside the solar system, moderated by the heliosphere to be essentially omnidirectional, with a peak energy around 300 MeV/u (corresponding to minimally ionizing particle energy), as shown in Figure 7. Because of the magnetoplasma effects of the solar wind in the heliosphere, the observed GCR flux at Earth orbit (1 AU from Sun) is variable based on solar activity, decreasing with an active Sun and increasing with an inactive Sun. This variability can be as much as an order of magnitude in particle flux. Also, there has been observed local anisotropic variability of the solar wind and GCR flux that is not completely understood (Gosling, 2007; Osman et al., 2012).

The Sun's contribution to the deep space radiation environment is the stream of ionized hydrogen and helium in a steady outgoing solar wind along with sporadic CMEs and SPEs. The solar wind energy peak is only 1 keV/u, but it has an intensity a billion times more than the GCR and is variable, depending on solar activity and distance from the Sun. The CMEs are pulses of hydrogen and helium plasma blasted from the Sun's corona in a directional cone, with peak energies on average 30 keV/u and intensities 3 times that of the solar wind. These blasts flow out from the Sun along a twisting spiral through interactions with the charged solar wind, forming fairly complex structures, as illustrated in Figure 8. The SPEs are much higher energy blasts, usually associated with x-ray flares, up to 100 MeV/u peak in energy, but of a moderate intensity between the solar wind and GCR. The number of 10-MeV particles detected is the typical measure of the SPE severity (Tribble, 2003).

TABLE I.—RELATIVE CONTRIBUTION OF PRIMARY GALACTIC COSMIC RAY (GCR) AND ALBEDO COMPONENTS TO TOTAL ABSORBED RADIATION DOSE AT LUNAR RECONNAISSANCE ORBITER (LRO) ALTITUDES
[Based on Spence et al. (2013).]

Radiation component	Percentage of total dose
GCR total	91.4
Protons	42.8
Heavy ions	30.1
Alpha particles, α (^{4}He)	18.5
Albedo total	8.6
Protons, p	3.1
Electrons, e^-	2.2
Positrons, e^+	1.5
Gamma rays, γ	1.1
Neutrons, n	0.7

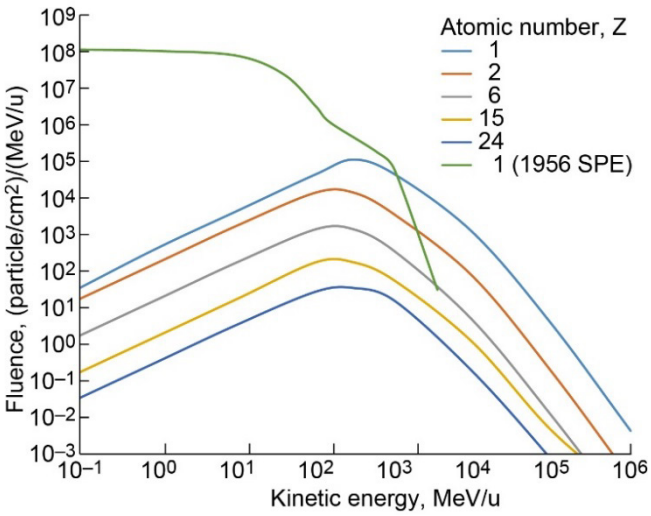

Figure 7.—Ion fluence spectrum; galactic cosmic ray annual fluence at solar minimum with total hydrogen fluence for strong solar particle event (SPE) occurring in February 1956 (based on Tribble (2010) and Wilson et al. (1997)).

TABLE II.—COMPONENTS OF DEEP SPACE RADIATION ENVIRONMENT AT 1 AU

Source	Description	Energy peak	Peak flux at 1 AU	References
Galactic cosmic rays (GCRs)	Stream of H+ to Fe+ (Z = 1→26)	~300 MeV/u	~0.1/u² to 1/u² particles/cm²·s	Clowdsley et al. (2005)
Solar wind	Stream of H+, He+ from Sun	~1 keV/u	~2 to 4×10^8 particles/cm²·s	Richardson and Wang (2003)
Coronal mass ejections (CMEs)	Pulses of H+, He+ from Sun	~30 keV/u	~3×10^9 particles/cm²·s	Low (2001); Savani et al. (2013)
Solar particle events (SPEs)	Pulses of H+, He+ from Sun	~10 to 100 MeV/u	~3×10^4 particles/cm²·s	Wilson et al. (1997)

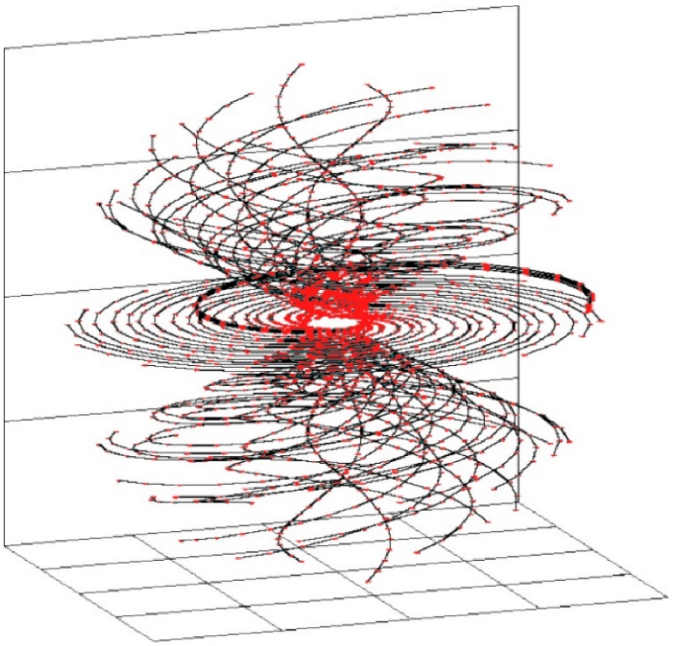

Figure 8.—Path of solar wind from Sun, generated by Energetic Particle Radiation Environment Model (EPREM) (modified from Schwadron et al., 2010; used with permission). Each division is approximately 4 AU.

4.0 Radiation Effects

When material is exposed to radiation, the radiation deposits energy into the material. The mechanism and effect of the interaction varies from type of radiation, its energy, and the material properties.

4.1 Radiation Dose

Exposure from radiation is typically reported in terms of "dose" and "dose equivalent." Dose refers to the energy absorbed from radiation sources per unit mass of a material. The SI unit of dose is the Gray (Gy), and is derived from deposited joules per kilogram (Thompson and Taylor, 2008). The dose equivalent is an indicator of effect or damage to a material relative to absorbed photons, calculated as the measured dose with a weighting factor (w_R) based on the type of radiation the material absorbs. The SI unit of dose equivalent is the Sievert (Sv). The conventional non-SI units of rad and rem for dose and dose equivalent, respectively, are still occasionally used, particularly in regulatory documents, and are derived from 100 ergs per gram using the CGS system. Likewise, there are 100 rad per Gray and 100 rem per Sievert for converting between the two systems.

The weighting factors for different types of absorbed radiation depend on the type of particle and, in the case of neutrons, the energy E_n as well. Table III shows the current recommended radiation weighting factors (Olive et al., 2014). In general, photon and electron doses are weighted at 1; proton, pion, and high-energy neutron doses are weighted at 2; and alpha particles α, fission fragments, heavy ions, and moderate energy neutrons are weighted up to 20.

TABLE III.—WEIGHTING FACTORS TO DERIVE DOSE EQUIVALENT FROM DOSE
[From Olive et al. (2014).]

Radiation type	Weighting factor w_R
Photons, electrons, muons	1
Protons, charged pions	2
Neutrons, $E_n < 1$ MeV	2.5 → 20
1 MeV < E_n < 50 MeV	20 → 5
$E_n > 50$ MeV	5 → 2.5
Alpha particles, heavy ions, fission fragments	20

The average dose equivalent exposure rates for various radiation environments are given in Table IV. On the Earth, dose rates begin to climb noticeably even in midaltitude aircraft compared to on the surface. Both astronauts and aircraft crews (civilian and military) operating at altitudes above 8 km (26,000 ft) are considered radiation workers by the Federal Aviation Administration (FAA) because of space radiation exposure. The dose rate at 12 km (40,000 ft) is about 20 times as on the ground, and at 18 km (60,000 ft) altitude the rates are double that. Polar routes can receive 3 times the exposure rate than equatorial routes, and an active Sun can increase dose rates in flight by a factor of 3 during energetic SPEs (Friedburg and Copeland, 2003; Uchihori et al., 2003).

4.2 Radiation Damage

The radiation environment can effect material by a number of ways (Olive et al., 2014). The most common effect is by ionization, where ions are created in a target material when a charged particle passes through it. Generally, ionization is when the charge particle pulls electrons (or pushes them if it is negatively charged) from the target material atoms through interactions of their respective electric fields. Another method of ionization is by direct collision, or knock-on interaction, which dislodges electrons or protons, and is not dependent on whether the incoming particle is charged or not, such as neutrons. The collision can also scatter incoming charged particles in a variety of directions depending on the momentum and geometry of the collision.

Gamma radiation can be absorbed by electrons in a target material, which would gain enough energy to escape their atomic bands and thus cause the material to be ionized. If the

TABLE IV.—AVERAGE DOSE EQUIVALENT EXPOSURE RATES FOR VARIOUS RADIATION ENVIRONMENTS

Radiation region	Average exposure rate (with shielding noted)	Reference
Terrestrial (surface background)	0.25 μSv/h	Olive et al. (2014)
Aircraft (at 12 km)	3.6 to 6.3 μSv/h	Friedberg and Copeland (2003)
International Space Station (ISS, at 400 km)	15 μSv/hr (3 mm Al)	Akopova et al. (2005)
Geosynchronous Earth orbit (GEO, at 35,800 km)	83 mSv/hr (3 mm Al)	Tribble (2003)
Deep space galactic cosmic rays (GCRs)	24 to 82 μSv/h	Simonsen (2000)
Deep space solar particle event (SPE)	→200 mSv/h	Simonsen (2000)
Europa (Jupiter orbit)	5 Sv/hr (1 cm H_2O)	Paranicas et al. (2009)

incoming gamma rays are of high enough energy, the radiation can also interact with the electric field of the atoms, causing the creation of an electron-positron pair through pair production. The mass of the created electron and positron is formed by the electric field from the energy of the gamma ray. Any amount of energy over the 1 MeV required to create the mass of the two leptons will be shared equally between the electron and position as kinetic energy. Of course, the electron and positron naturally attract each other electrostatically, so unless they interact with the target material first, they can annihilate each other forming two secondary gamma rays.

In a process called bremsstrahlung, or breaking radiation, a moving charged particle is deflected by the target material or by an external electromagnetic field. To conserve the change in momentum, photons are radiated by the deflected particle. Similarly, Cherenkov radiation is caused by a charged particle traveling faster than the allowed propagation of electric fields in the target material. The interference of the moving charge with the field in the target material results in a shock wave of photons radiated from the traveling particle, similar to that of a sonic boom that forms when an aircraft or meteor moves faster than sound in air.

The absorption of space radiation by the nuclei of target material may also cause creation of secondary radiation due to transmutation of the target nuclei or the nuclear spallation of the atom. Dislocations or voids may be created as the material is deformed by the motion of the atoms when the nuclei of the target material absorbs some of the radiation. Another secondary effect is surface charging when the ionized material cannot distribute the accumulated charge from ionization, which can cause significant problems for spacecraft electronic components.

If a target material is not conductive, ionization effects will cause the surfaces to become charged over time. For example, regolith surfaces to a depth of 1 mm (subsurface) charges up to 700 V/m by GCR ions, and large SEP events charge 1,000 times that (Budenstein, 1980; Frederickson, Cotts, and Wall 1986). These large local fields may lead to dielectric breakdown along grain boundaries and inclusions, causing plasma etching of the surface and affecting physical, chemical, and optical characteristics (Campins and Krider, 1989; Balmain, 1987).

5.0 Radiation Risks to Space Science Instrumentation Technologies

Space science instrumentation systems are exposed to radiation environments in some ways more severe than Earth-based instrumentation. Earth-based instrumentation has to contend with muons from cosmic ray showers and gamma rays from decay products deep under the ground. In space, as outlined above, the instrumentation is thrown into a variable radiation environment dependent on locale, with limited communications and infrastructure support. Space science necessarily forces instrumentation and supporting electronics exposure to this harsh radiation environment.

5.1 At-Risk Instrumentation Components

Thermocouples and thermopiles are commonly used in radiometers and bolometers; they also measure temperatures of system components. Their signals are produced by comparing the electric potential difference generated between two different conductors over a thermal gradient. Since they are dependent on material quality and electrical isolation, errors can be produced by irradiation either through impurities introduced either by transmutation of the conductors, which heats from energy deposited by the space radiation through ionization, or by induced charging from ionizing particles (Boland, 1970). The modification of thermocouple calibration by radiation is primarily though the absorption of secondary neutrons causing transmutation; those thermocouple alloys with smaller Z will be less susceptible to those effects. From theoretical and experimental studies, the ANSI Type K Chromel-Alumel thermocouple is considered the most stable of the metal thermocouples (Boland, 1970). Of high-temperature ceramic thermocouples, zirconium carbide, chromium disilicide, and

molybdenum disilicide are expected to be the most resistant to radiation effects (Wrbanek et al., 2004).

Thermistors, resistance temperature detectors (RTDs), and any resistor-based transducer that utilizes a bridge circuit are also subject to radiation effects. Not only are the resistors subject to modification by transmutation and/or ionizing heating that affect the measurements, but also the impacting charge particles will induce currents in the bridge circuits (Boland, 1970).

Capacitive sensors, sensors utilizing a capacitor for measurement such as pressure, are also affected by radiation. The measurement is based on the monitoring of voltage changes in a capacitor that has changes in the electrode spacing or dielectric material between the electrodes. The capacitor electrodes can gain charge from ionizing particles and thus read an induced voltage in the measurement. If the sensor has a dielectric between the electrodes, under irradiation it will become more conductive upon collecting ionizing charges, causing the device to increase its dissipation factor and decrease sensitivity (van Lint et al., 1980).

Photosensitive devices such as optical photodiodes produce a signal through photoelectric effects. These effects are also imitated by radiation, either through ionization or by photoelectric effects of secondary gamma radiation. Damage to the device structure by radiation-induced displacement also forms localized regions of carrier recombination, which reduces the sensitivity of the devices. Similarly, nonsensing diodes experience increased radiation-induced current as well as displacement damage, which increases the resistance of the diode material (van Lint et al., 1980).

Transistors used in signal processing or system operational electronics are effected by space radiation as well. Gain of transistor-based amplifiers are affected by displacement effects through increase of the semiconductor resistivity and increased carrier recombination in localized dislocation sites. Photoelectric effects of radiation also increase leakage current. In particular, metal-oxide-semiconductor (MOS) devices also are affected by charge formation in the insulator (oxide), which drift to the insulator-semiconductor interface, causing an increase in bias voltages and increasing the susceptibility of single-event effects such as single-event upsets (SEUs) (van Lint et al., 1980).

5.2 Observed Damage

Many studies exist of radiation damage under in-space conditions in LEO (Tribble, 2010; Underwood, 1998). The degradation is seen as a logarithmic function, such that the damage to the device is dependent on how much damage the device has already taken aside from the dose absorbed. For example, the degradation of the efficiency of solar cells on the ISS is shown in Figure 9. In another example, the SEU rate of memory on Earth-orbiting satellites is shown in Figure 10 and has a similar behavior.

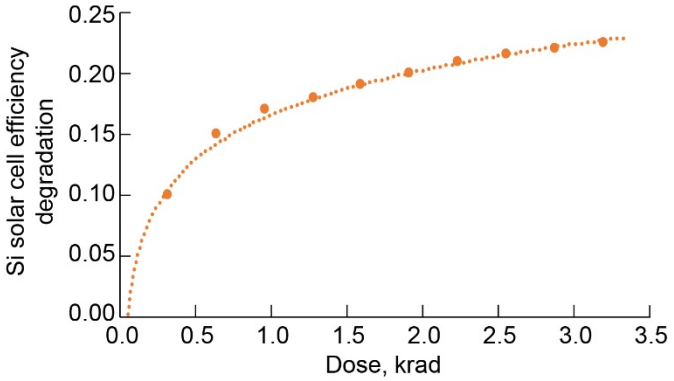

Figure 9.—Silicon solar cell power loss versus radiation exposure at 700 km altitude, 30° inclination orbit, and 320 rads per year (estimated) on International Space Station (after Tribble (2010)). This includes estimated 0.015 degradation per krad of 5-mil coverglass. A logarithmic curve fit to data is also shown.

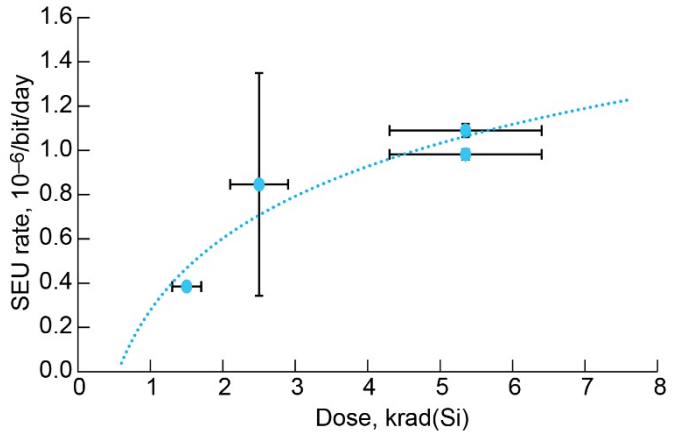

Figure 10.—Single-event upset (SEU) rate in low Earth orbit versus estimated dose for onboard computer memory on satellites (after Underwood (1998)). Logarithmic curve fit to data is also shown.

5.3 Single-Event Upset Mechanisms

The processes for initiating single-event effects are believed to be reactions due to bombardment of protons or neutrons and the subsequent release of secondary charged particles.

One approach to model SEU rates (Petersen, 1980; Petersen, 1992) estimates the upset rate as inversely proportional to the Bendel parameter (A_b), the proton incident energy threshold for reactions that produce upsets. The parameter is itself calculated as the sum of the threshold energy for proton capture and transmutation of the semiconductor to generate a charged

particle of threshold energy (E_{th}), and adding the deposited energy of the secondary particle (dE/dx) in the target material thickness (T), as shown in Equation (1).

$$A_b = E_{th} + \frac{\mathrm{d}E}{\mathrm{d}x}T \tag{1}$$

The main bombardment reaction cited in this approach is ^{28}Si(p, α)^{25}Al, with other reactions ^{28}Si(p, 2p)^{27}Al and ^{28}Si(p, α+p)^{24}Mg cited as well, but with less impact on upset rates because of higher threshold energies.

The threshold energy for proton capture reactions for various elements used in microelectronics is given in Table V as well as their Q values, the difference between the energy-equivalent masses of the incoming and outgoing particles. A negative threshold energy is indicative of a lack of a minimum energy for proton capture. A positive Q value is indicative of an exothermic reaction. The dE/dx in megaelectronvolts per micrometer for secondary 5.5-MeV alpha particles in the bulk target material as determined using the radiation transport program SRIM (Stopping and Range of Ions in Matter; Ziegler, Ziegler, and Biersack, 2010) is also given in the table. The Bendel parameter apparently is dominated by the threshold energy for low-Z elements, and by dE/dx for high-Z elements. Given the inverse relationship between the upset rate and the Bendel parameter, the higher Z elements would appear to be more susceptible to upsets.

Another approach (Chadwick and Normand, 1999) is to relate the SEU rates with the total cross sections of incoming particles to derive a "burst generation rate" (BGR). The BGR is a function of recoil energy for specific incoming particle energy, integrated for all inelastic and elastic reactions. The (p,α) reactions typically dominate, and as an indicator of how these cross sections vary, the total neutron cross section from the standard nuclear data library ENDF (evaluated nuclear data file) (Brown et al., 2011) corresponding to the individual elements at 20 MeV is also given in Table V (in barns; 1 b = 10^{-28} m²).

The stresses from dislocations and voids created in semiconductor devices through radiation damage can be reversed by annealing. However, as noted earlier, creation of charges through ionization effects along nonconducting surfaces or interfaces can cause significant localized voltage buildup, resulting in catastrophic dielectric breakdown through grain boundaries, defects, and voids and making affected electronic devices unrecoverable.

TABLE V.—THRESHOLD ENERGIES, Q VALUES, AND ENERGY TRANSFER FOR SECONDARY 5.5-MeV ALPHA PARTICLES OF (p,α) REACTIONS AND NUCLEON CROSS SECTIONS FOR VARIOUS ELEMENTS USED IN MICROELECTRONICS

(p,α) reaction	Threshold energy, E_{th}, MeV	Q value, MeV/c^2	Deposited energy, dE/dx,[a] MeV/μm	Cross section,[b] σ_n, b
11B(p,α)9Be	–3.15	+9.10	0.166	1.38
12C(p,α)9B	14.41	–7.04	0.170	0.44
14N(p,α)11C	9.36	–2.41	0.075	1.55
16O(p,α)13N	11.78	–4.71	0.099	1.64
27Al(p,α)24Mg	4.59	+2.11	0.154	1.82
28Si(p,α)25Al	14.24	–7.20	0.133	1.87
31P(p,α)28Si	4.27	+2.43	0.101	1.71
64Zn(p,α)61Cu	5.40	+1.35	0.288	2.60
69Ga(p,α)66Zn	1.76	+4.95	0.228	2.86
74Ge(p,α)71Ga	4.67	+2.09	0.204	2.69
75As(p,α)72Ge	1.78	+4.93	0.210	2.85
115In(p,α)112Cd	0.30	+6.42	0.229	3.69
181Ta(p,α)179Hf	–2.65	+9.38	0.391	4.46

[a]For secondary 5.5-MeV alpha particles.

[b]At 20 MeV.

5.4 Defect Formation

Defects in the materials are formed by the changes in atomic and molecular bonds in the semiconductor caused by the deposition of ionizing radiation as well as by the direct displacement of atoms by deposited energy or knock-on interactions. The displacement energy, or the energy to form a defect in a material, is thus a measure of radiation hardness, but is also affected by the presence of impurities, dopants, and existing defects.

Displacement energies of materials are typically measured by the irradiation of test samples in particle beams. For those materials whose data are not available, computational simulations have been developed using rough approximations to detailed maps of crystallographic potentials (Williford, Devanathan, and Weber, 1998). In comparing the formation of defects formed between materials, and thus relative radiation hardness, the nucleon displacement cross section as well as the displacement energy are useful metrics (Nordlund, et al., 2015).

Displacement energy is proportional to the cross-sectional area of the defect given by the square magnitude of the Burgers vector (which in itself is proportional to the average lattice size), the elastic modulus, and the depth of the dislocation perpendicular to the Burgers vector (on the order of the lattice size). Thus, comparing the lattice size and the elastic modulus gives an estimate of relative displacement energy. Table VI summarizes the properties of semiconductors and insulators used in microelectronics subject to space radiation damage.

TABLE VI.—PROPERTIES OF SEMICONDUCTORS AND INSULATORS USED IN MICROELECTRONICS EXPOSED TO SPACE RADIATION[a]

Property	Si	SiC (4H)	Diamond (sp^3 C)	GaAs	GaN	GaP	InAs	InP	BN	ZnO	SiO_2	Si_3N_4	Sapphire (α-Al_2O_3)
Atomic number, Z	14	14+6	6	31+33	31+7	31+15	49+33	49+15	5+7	30+8	14+(2×8)	(3×14)+(4×7)	(2×13)+(3×8)
Band gap energy, E_g, eV	1.12	3.08	5.48	1.42	3.39	2.26	0.36	1.35	6.4	3.35	9	5.3	8.8
Electron-hole (e-h) pair creation energy, eV	3.63	6.9	13.1	4.35	8.9	6.54	-------	-------	--------	7.50	----------	----------	----------
Deposited energy, dE/dx (MIP),[b] eV/μm	386	542	396	732	896	770	748	650	597	833	462	572	678
Density, g/cm³	2.329	3.2	3.515	5.317	6.15	5.3	5.68	4.81	3.45	5.606	2.66	3.31	3.98
Lattice size, Å	5.431	3.08; 10.053	3.5668	5.653	3.187; 5.187	5.45	6.05	5.86	3.6157	4.58	5.15; 13.86	7.64; 2.91	4.785; 12.991
Elastic modulus, GPa	130 to 185	450	1,050	85.9	181	103	51.4	61.1	748	140	57 to 75	317	250 to 400
Displacement, eV	18 to 25	21	43	10	15	-------	-------	-------	--------	-------	----------	----------	----------

[a]From Sellin and Vaitkus (2005); Siklitski et al. (2001); Bermudez (2005); Robertson and Falabretti (2006); Ceramic Industry (2013); MolTech GmbH (2013); Ziegler, Ziegler, and Biersack (2010).

[b]MIP = minimally ionizing proton; dE/dx calculated from program SRIM (Stopping and Range of Ions in Matter) for a 2.5-GeV proton in each semiconductor.

Of the wide-band-gap (WBG) semiconductors, SiC and diamond have high displacement energies—about twice of that of silicon. Electronics and detectors based on SiC and diamond are fields of active research and are becoming accepted solutions for high-temperature and high-radiation environments (Juhasz, Tew, and Schwarze, 1998; Sellin and Vaitkus, 2005; Khon and Denisenko, 2007; Bachmair, 2016). Boron nitride is also expected to have a high displacement energy based on its lattice size and elastic modulus. Of the insulators, Si_3N_4 and sapphire are expected to have displacement energies at nearly 3 times that of SiO_2.

5.5 Radiation-Hard Electronics Development

Instrumentation signal conditioning is dependent on transistor-based operational amplifiers. Two commonly used transistors are JFETs and MOSFETs, schematically shown in Figure 11. The JFET (junction field effect transistor) is a p-n junction transistor with source and drain terminals on the p-doped region of the semiconductor and a gate terminal bonded directly to an n-doped region with a depletion region formed between them. The MOSFET (metal-oxide-semiconductor field effect transistor) has the source and drain terminals bonded to its own (lightly doped) n-region and the gate terminal bonded to a thin oxide layer over a more heavily doped n-region. The MOSFET design allows very low current operation of logic or control circuits, but is more susceptible to irreversible radiation damage, particularly to the oxide layer, than the JFET. The insulator and one pole on the gate terminal makes the MOSFET more susceptible to radiation damage effects.

The low nucleon cross section of carbon seen in Table V and the high displacement energy of SiC seen in Table VI makes SiC an ideal semiconductor for radiation environments compared to silicon and other WBG semiconductors. Diamond—because it is pure carbon—may also be a useful WBG semiconductor. The large displacement energies of Si_3N_4 and sapphire makes the inclusion of these materials attractive as insulation to improve the radiation hardness of electronics.

To enable advanced jet engine ground tests and prolonged data collection from planetary surfaces, NASA Glenn Research Center has been developing the technology to extend the operating temperature envelope of transistor integrated circuits (ICs) well above the effective 300 °C limit of silicon-on-insulator technology (Larkin et al., 1994; Neudeck, 1994). Recently, stable operation of a 4H-SiC JFET IC fabricated with two levels of interconnect was demonstrated over 1,000 h at 500 °C (Spry et al., 2016). Based on the SiC JFET, these ICs are also expected to survive harsh radiation environments.

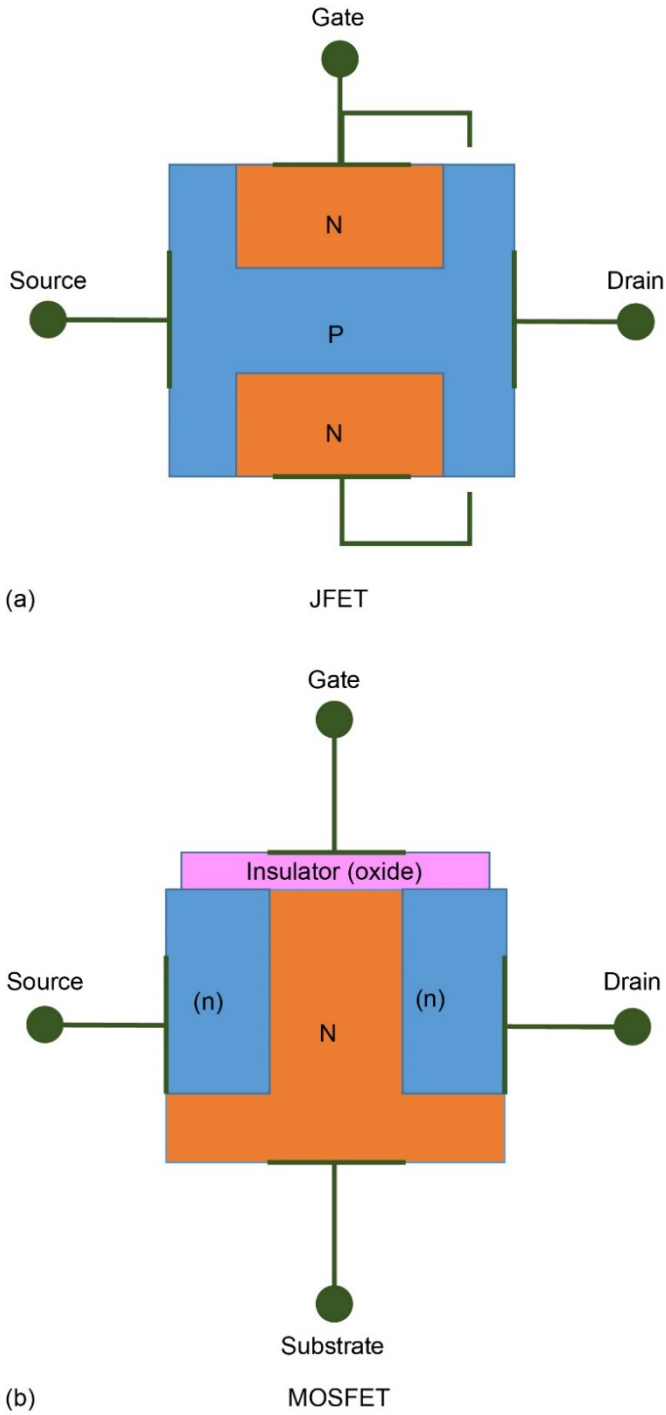

Figure 11.—Common transistors in amplifiers used for space science instrumentation. (a) Junction field effect transistor, JFET. (b) Metal-oxide-semiconductor field effect transistor, MOSFET.

A packaged IC before and during a 650 °C test is shown in Figure 12. As a demonstration of the robustness of SiC with harsh environment packaging, a SiC JFET was operated on an exposure experiment platform mounted to outside the ISS for 9,778 h with less than 5 percent drop in drain current measured after exposure to an estimated 360 rad (Si) (Chen et al., 2013).

Ground tests irradiating silicon carbide devices have also been performed by NASA and other agencies. A set of SiC JFETs were tested (McGarrity et al., 1992) at Harry Diamond Laboratories (Adelphi, MD) with gamma ray exposure of up to 100 Mrad (Si) from a ^{60}Co source and at the Army's Aberdeen Pulsed Reactor Facility with exposed neutron fluence up to 10^{16} n/cm² (1 MeV equivalent in Si). There was an observed 15-percent decrease of drain current after gamma ray exposure, but the effect did not correlate with total dose. The mobility was affected by neutron fluence dropping between 3.5 percent at 10^{15} n/cm² and 26 percent at 10^{16} n/cm², reported to be about a third of what would be expected for silicon.

The Jet Propulsion Laboratory tested (Scheick, Selva, and Becker, 2004) reverse-biased SiC diodes with 63 MeV protons and ions of Li, F, Br, and I with energies 99 to 329 MeV. No breakdowns were seen with proton fluences less than 9×10^{11} p/cm² on biased diodes. The tests found immediate single-event breakdowns (SEBs) using the Br and I ions, with linear energy transfer (LET) >10 MeV·cm²/mg in SiC.

As part of the NASA Electronic Parts and Packaging Program, SiC MOSFET device performance was evaluated (Patterson et al., 2013) after gamma ray exposure at NASA's Goddard Space Flight Center. These tests found similar performance loss of less than 5 percent shift of the drain to source resistance after 600 krad (Si) exposure. The gate threshold voltage dropped for those devices under bias while irradiating, but was restored after annealing.

6.0 Space Science Radiation Detector Development

In order to provide a complete understanding of how energetic processes internal and external to the solar system shape magnetospheres, atmospheres, and surfaces, in situ particle observations should include measurements of GCRs, SPEs, CMEs, solar wind, and ion plasma. Missions to achieve these measurements would include flexible path orbiters, probes, landers, or rovers beyond LEO.

SmallSats with mass less than 100 kg (such as CubeSats) are seen to be low-cost platforms ideal for conducting this range of observations either solo or in multiple locations as a swarm. However, current detector technology limits the measurement capability by restrictions to size, power, and thermal stability of the SmallSat platform.

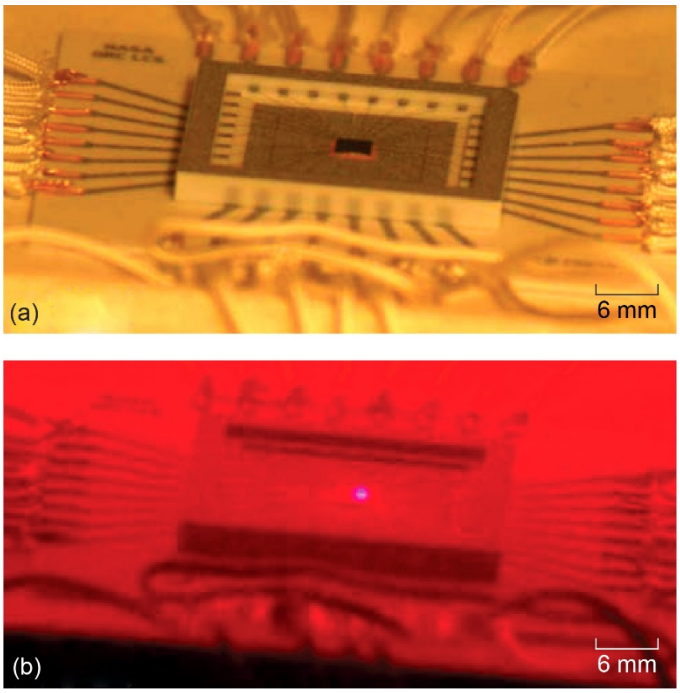

Figure 12.—Packaged integrated circuit device. (a) Before testing. (b) Testing at 650 °C with 4H-silicon carbide (SiC) junction field effect transistor (JFET) under forward bias of gate-channel junction, resulting in blue light emission (Spry et al., 2016).

6.1 Technology Limitations

Current radiation detector technology is limited in lifetime, precision, discrimination, and directional sensitivity for the mass, power, and volume requirements for future missions. Miniaturizing and integrating instrumentation is a high priority for addressing the challenges of crewed and uncrewed deep space missions to high Earth orbit (HEO), near-Earth objects (NEOs), lunar and Martian orbits and surfaces, and outer planetary systems as well as for improving high-altitude aircraft safety (National Research Council, 2012a).

Advanced instrumentation technology for space radiation applications is specifically called for in the "NASA Strategic Program Plan for Space Radiation Health Research" (NASA OLMSA, 1998). Technology requirements are defined by the National Research Council's "NASA Space Technology Roadmaps and Priorities" (National Research Council, 2012b), the "NASA Science Instruments and Sensor Capabilities Road Map" (NASA Science Mission Directorate, 2005), and the design goals of existing cosmic-ray detectors (National Research Council, 2008). These requirements include particle energy range and resolution, angular coverage and resolution, and the number of sensing elements as important design criteria in trade studies.

Current state of the art (SOA) in solid-state space radiation detectors derive from Earth-based applications. The challenge

has been to optimize the existing technology from the nuclear laboratory to fit space-based science platforms. However, the increasing demand for instruments to fit the low size, power, and cost restrictions of small satellite platforms forces a reconsideration of this approach.

Cherenkov detectors typically comprise an ultraviolet- (UV-) transparent radiator material bonded to a UV-sensitive photomultiplier tube (PMT). These PMTs typically are limited in operating temperatures, require high voltage and moderate power levels, and are fairly bulky—usually larger than the radiator material in space-based systems.

For LET detectors, the current SOA utilizes silicon PIN or lithium-drifted silicon diodes. The size of the detectors varies from 1 mm^2 to several square centimeters in active area. Because of the use of silicon as the semiconductor, these devices' dark currents have considerable sensitivity to temperature and require some form of temperature control or compensation to reduce noise.

Scintillation detectors typically comprise a scintillating material bonded to a PMT that is sensitive to the wavelength emitted by the scintillators. The scintillators, plastic or crystal, are typically limited in temperature, and the PMTs have the limits noted above. Recently, the use of avalanche photodiode (APD) arrays as replacements to PMTs have resulted in less power consumption in a smaller package (O'Neill et al., 2013). However, these devices currently have small active areas and are subject to large temperature sensitivities in dark current and thus require active temperature compensation to reduce noise.

Using a CubeSat as a payload design point (1,000 cm^3, 1.33 kg), implementing a full-field radiation detector system using the current SOA devices is not realistic. Current SOA technologies rely on temperature compensation and/or regulation for proper operation. Also, planned future usage for small satellites in deep space where there is high radiation particle flux makes the silicon-based detectors more susceptible to radiation damage, particularly as large-area devices. The large volume needed for PMTs (more than 100 cm^3) makes the application of any solid-state device (less than 10 cm^3) preferable for a small satellite platform.

6.2 Future Full-Field Detector System Concept

To meet the challenges of low-power, low-noise, multidirectional robust detectors for a wide range of mass and energies, new ion detectors based on WBG semiconductors are being developed. Potential technologies for this detector system have been identified and demonstrated for lower power, more compact detector components.

These technologies are being applied to develop a Compact Full-Field Ion Detector System (CFIDS) (Wrbanek, Fralick, and Wrbanek, 2011; Wrbanek, Fralick, and Wrbanek, 2012; Wrbanek, Wrbanek, and Fralick, 2013; Wrbanek and Wrbanek, 2016). The CFIDS is designed to be an extremely compact low-cost instrument, capable of being flown on a wide variety of deep space platforms, to provide multidirectional, comprehensive (composition, velocity, and direction) in situ measurements of heavy ions in space plasma environments.

The CFIDS comprises a central spherical Cherenkov detector surrounded by detector stacks of LET detectors as well as coincidence and anticoincidence (trigger and veto) detectors for signal processing. A design concept for this technology approach is illustrated in Figure 13. To enable this concept, advancements have been made in radiation detector technology using WBG semiconductor devices. With less physical and electrical demands on science platforms, the instrument can be flown on CubeSats and other small satellite platforms beyond LEO.

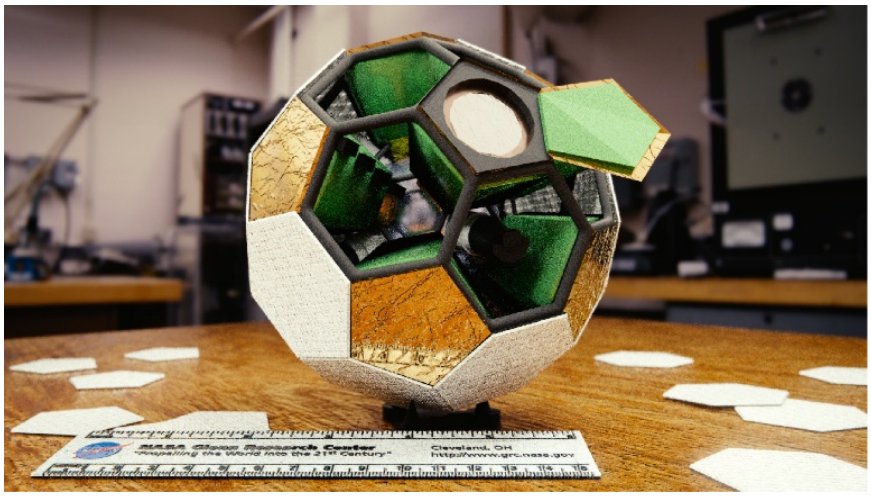

Figure 13.—Design concept of Compact Full-Field Ion Detector System (CFIDS) assembly (cables and signal conditioning hardware not shown for clarity) (Wrbanek and Wrbanek, 2016).

The advanced design of CFIDS maximizes collection area and improves sensitivity, yet maintains an ultracompact design, unlike systems, which rely on optics and typically greater volume to improve sensitivity, and thus allows simultaneous coverage of the entire sky.

6.3 Radiation Detector Technology Development

To meet the challenges of low-power, low-noise, multidirectional robust detectors for a wide range of mass and energies, new radiation detectors based on WBG semiconductors are being developed at Glenn for integration into SmallSat platforms (Wrbanek and Wrbanek, 2016).

6.3.1 WBG LET Detectors

The application of SiC for LET detectors is based on the material's WBG and high displacement energy. These properties give several advantages over silicon-based detectors. Sensors and electronic devices made from SiC have much better resistance to radiation damage from energetic charged particles that can form defects in the semiconductor (Nava et al., 2008). The WBG nature of SiC also allows measurements made by the detectors to be unaffected by thermal drift due to Sun-shade transitions.

Microelectromechanical-system- (MEMS-) based devices fabricated from SiC for the purpose of conducting low-noise neutron and alpha particle spectrometry have been reported in the context of reactor core monitoring (Ruddy et al., 1998). A low-power, low-mass space radiation detector prototype system using a SiC Schottky power diode was developed at Glenn for dosimetry use during future lunar missions (Wrbanek et al., 2007). Recently two large-area (200-mm²) SiC radiation detectors based on high-purity semi-insulating (HPSI) SiC were fabricated and demonstrated as proof-of-concept devices, shown in Figure 14.

A bench check of the capacitance and leakage current of the HPSI SiC detectors revealed that they had electrical characteristics comparable to much smaller silicon PIN diode detectors (with 2 percent of the active detection volume of these SiC detectors). The detector capacitances averaged 65±5 pF, with leakage currents of 4.5 nA at 100 V, corresponding to an estimated carrier concentration of 1.24×10^4 cm^{-3}.

Exposure of the detectors to alpha particle sources revealed significant sensitivity to external electromagnetic interference (EMI), which was traced to the leads between the detector and charge amplifier. The gamma ray spectrum of the sources was seen in the background noise of the detectors at high gain (550×) on the multichannel analyzer (MCA). Blocking the background in the MCA software, an alpha particle signal was seen at low gain (3.1×).

The recorded spectra with background and peaks labeled are seen in Figure 15 and Figure 16. The peak widths are seen on average to reflect $dE/E = 0.20$. These peaks were greatly affected by EMI, with energy spreading because of the wide 5-cm² sources and the airgap between the detector and source.

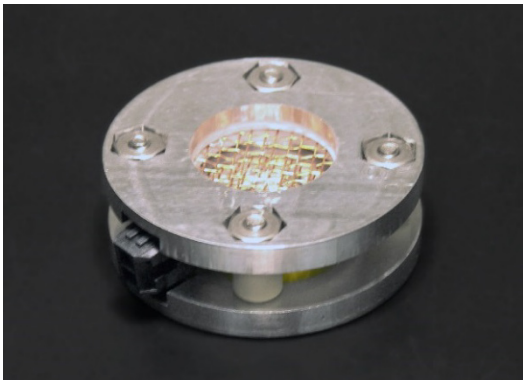

Figure 14.—Large-area (2-cm²) SiC radiation detectors, fabricated and assembled (Wrbanek and Wrbanek, 2016).

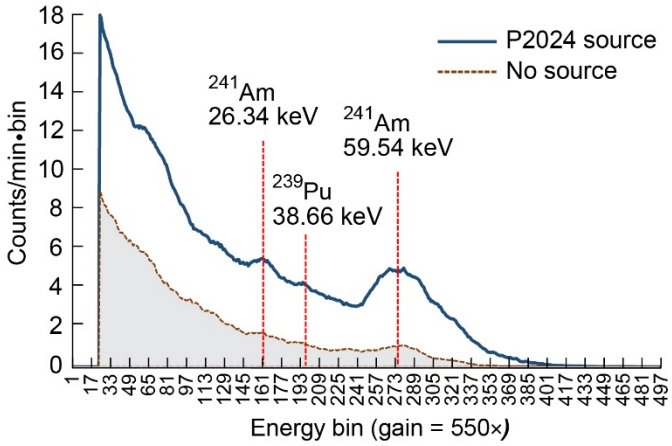

Figure 15.—Reaction of large-area SiC linear energy transfer (LET) detector to gamma rays emitted from ^{239}Pu source.

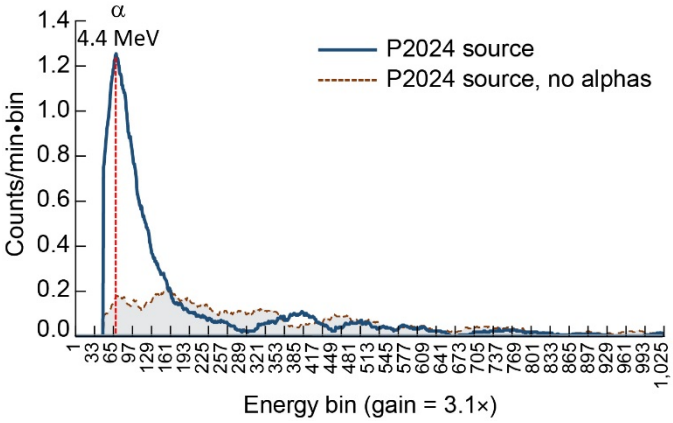

Figure 16.—Reaction of large-area SiC linear energy transfer (LET) detector to alpha particles emitted from ^{239}Pu source.

Figure 17.—Miniature scintillation-diode ionizing radiation detector as demonstrated (Wrbanek and Wrbanek, 2016).

6.3.2 Solid-State Coincidence and Anticoincidence Detector

Spacecraft-based coincidence and anticoincidence (trigger and veto) detectors generally comprise scintillator blocks of plastic or iodide crystal mated to a PMT or a pixelated APD detector, also referred to as a silicon photomultiplier (SiPM). The goal is to replace the role of PMTs and SiPMs in these types of detectors with WBG devices, saving on size, weight, and required power.

A miniature "paddle style" radiation detector was demonstrated using a GaP photodiode mated to a polyvinyl toluene (PVT) scintillator block as shown in Figure 17 (Wrbanek and Wrbanek, 2016; Wrbanek, Wrbanek, and Fralick, 2019). The preliminary results indicate that the improvement in required size and power with the use of the WBG material, and if used with acrylic ribbon scintillators, allows its use in the CFIDS concept.

6.3.3 Solid-State Cherenkov Detector

At the heart of the detector system concept is a spherical Cherenkov detector. Typical Cherenkov detectors comprise flat disks or blocks of sapphire or acrylic mounted on PMTs. The goal is to replace the role of the relatively large PMTs with solid-state devices that do not require temperature control or compensation.

A fast, large-area solid-state UV detector based on the WBG semiconductor ZnO has been recently developed at Glenn (Wrbanek and Wrbanek, 2016; Wrbanek and Wrbanek, 2018). The proof-of-concept detector was fabricated on commercially available bulk single-crystal undoped ZnO. Interdigitated finger electrodes and contact pads were patterned via photolithography and formed by sputtered silver, as shown in Figure 18. The device tested had an active area of 1 by 2 mm (2 mm^2), designed to have a 1-ns response time with 10 V applied bias voltage. In a bridge circuit, the detector would detect small, fast pulses of UV light such as those required for Cherenkov detectors.

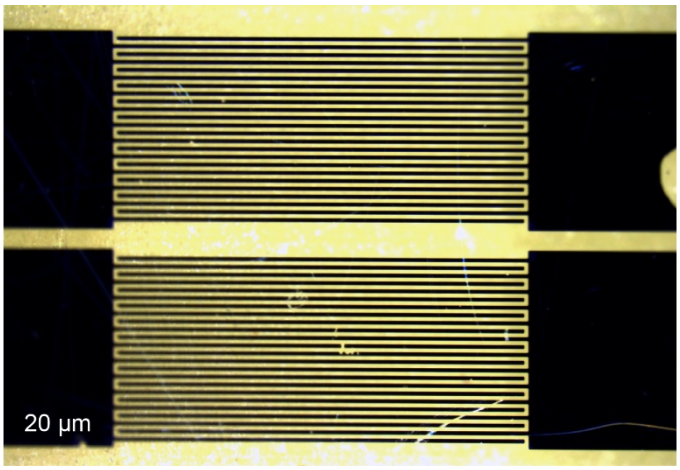

Figure 18.—Proof-of-concept ZnO ultraviolet (UV) detectors with 20 µm electrode spacing. The sizes of the interdigitated finger areas are 1 by 2 mm (Wrbanek and Wrbanek, 2016).

The ZnO-based detector was demonstrated to be sensitive to UV light at 254 nm, slightly less so at 370 nm, and not sensitive to room lighting (about 430 to 630 nm). Compared to commercial SiC and GaP detectors tested in parallel, this detector also demonstrated greater sensitivity to UV than the existing devices.

TABLE VII.—COMPARISON OF ESTIMATED PROPERTIES FOR STATE-OF-THE-ART (SOA) AND PROPOSED COMPACT FULL-FIELD ION DETECTOR SYSTEM (CFIDS) DETECTORS

Detector	Active area	Mass	Volume	Voltage	Dark current	Minimum power draw	Maximum signal to noise	Maximum operating temperature	Fractional temperature sensitivity of dark current
Linear energy transfer detectors									
SOA: Si PIN	1 cm^2	0.5 g	185 mm^3	100 V	5 nA	0.5 μW	1×10^5	60 °C	0.20/°C
Si(Li)		35 g	15 cm^3	300 V	5 μA	1.5 mW	2×10^4	60 °C	0.30/°C
Proposed: SiC	2 cm^2	0.5 g	113 mm^3	100 V	5 nA	0.5 μW	1×10^5	120 °C	0.001/°C
Scintillator coincidence/anticoincidence detectors									
SOA: [a]PMT	20 cm^2	170 g	180 cm^3	1,000 V	5 nA	5 μW	4×10^4	50 °C	0.002/°C
[b]APD	9 mm^2	3 g	200 mm^3	30 V	5 nA	0.15 μW	8×10^4	85 °C	0.30/°C
Proposed: GaP	4.8 mm^2	5 g	170 mm^3	5 V	20 pA	0.1 nW	3×10^5	125 °C	0.005/°C
Cherenkov detectors									
SOA: PMT	20 cm^2	170 g	180 cm^3	1,000 V	5 nA	5 μW	4×10^4	50 °C	0.002/°C
Proposed: ZnO	2 mm^2	11 g	0.80 cm^3	10 V	5 nA	0.05 μW	4×10^4	125 °C	0.0005/°C

[a]PMT is photomultiplier tube.

[b]APD is avalanche photodiode.

6.3.4 Technology Comparison

A comparison of properties of SOA and proposed active elements for application as CFIDS detectors is shown in Table VII. From this summary, it can be seen that WBG devices provide significant improvements in power and performance over conventional SOA devices. Thus, the CFIDS system will not depend on temperature compensation and will significantly reduce noise at lower power usage while increasing tolerance to radiation damage.

7.0 Concluding Remarks

The space radiation environment is a subject of ongoing study in a variety of space science fields. Understanding the interactions for the Sun, Earth, and other natural and man-made objects in the solar system with the space radiation environment helps provide answers to compelling science questions and provides crucial knowledge to improve robotic space missions and manned spaceflights.

The local space radiation environment created by the interaction of cosmic rays with the planetary surfaces, atmospheres, and magnetic fields is dependent on the physical environment, producing a variety of effects. These effects are variable, based on the type and energy of radiation as well as the material exposed. In situ instrumentation for the exploration of air and space is particularly at risk because of its direct exposure to the variable radiation environment without direct infrastructure support.

To conduct the in situ measurements of the space-radiation environment on small, low-cost platforms such as small satellites, the current detector technologies have limited capabilities. Advanced space-science instrumentation technologies are needed to meet the goals to improve particle energy range and resolution, angular coverage and resolution, and the number of sensing elements.

Development of wide-band-gap (WBG) semiconductors as radiation detectors holds the promise of improved low-power, robust radiation detectors. New ion detectors based on WBG semiconductors are being developed at NASA Glenn Research Center to enable a compact full-field ion detector system for space science on a CubeSat platform. Potential technologies for this detector system have been identified and demonstrated for lower power, more compact detector components.

Appendix—Nomenclature

α	alpha particle, He nucleus
σ_n	nuclear cross section (b)
A_b	Bendel parameter (MeV)
ACR	anomalous cosmic ray
AMS	Alpha Magnetic Spectrometer
APD	avalanche photodiode
AU	astronomical unit (approximate distance of the Earth to Sun, or 149,597,870 km)
b	barn; cross-section unit (10^{-28} m^2)
BGR	burst generation rate
CFIDS	Compact Full-Field Ion Detector System
CME	coronal mass ejection
CP	charge conjugation parity symmetry (i.e., antimatter being a mirror of matter)
dE/dx	deposited energy (MeV/μm)
E_g	band gap energy (eV)
EMI	electromagnetic interference
E_n	energy of a neutron (MeV)
ENDF	evaluated nuclear data file
EPREM	Energetic Particle Radiation Environment Model
E_{th}	threshold energy (MeV)
eV	electronvolts (1 eV = 1.602×10^{-19} J)
FAA	Federal Aviation Administration
FGST	Fermi Gamma-ray Space Telescope
GCR	galactic cosmic ray
GEO	geosynchronous Earth orbit (altitude of 35,786 km)
GeV	giga-electronvolts (1 GeV = 1.602×10^{-10} J)
Gy	Gray, unit of absorbed dose (J/kg)
HEO	high Earth orbit (altitude greater than 35,786 km)
HPSI	high-purity semi-insulating (semiconductor)
IC	integrated circuit
ISS	International Space Station
JFET	junction field effect transistor
LEO	low Earth orbit (altitude less than 2,000 km)
LET	linear energy transfer (MeV·cm²/mg)
LRO	Lunar Reconnaissance Orbiter
MCA	multichannel analyzer
MEMS	microelectromechanical systems
MEO	middle Earth orbit (altitude between 2,000 and 35,786 km)
MeV	mega-electronvolts (1 MeV = 1.602×10^{-13} J)
MIP	minimally ionizing proton (with energy about 2.5 GeV)
MOS	metal oxide semiconductor
MOSFET	metal-oxide-semiconductor field effect transistor
n	neutron
NEO	near-Earth object
p	proton
PMT	photomultiplier tube
PVT	polyvinyl toluene
Q	energy difference between primary and secondary particle energies (MeV)
rad	unit of absorbed dose (0.01 Gy)
R_E	Earth radius (6,371 km)
rem	roentgen equivalent man, unit of equivalent dose (0.01 Sv)
RTD	resistance temperature detector
SCD	sudden cardiac death
SEB	single-event breakdown
SEP	solar energetic particle
SEU	single-event upset
SiPM	silicon photomultiplier
SNO	Sudbury Neutrino Observatory
SOA	state of the art
SPE	solar particle event
SRIM	Stopping and Range of Ions in Matter (software)
Sv	Sievert, unit of equivalent dose (J/kg)
T	target material thickness (μm)
u	unified atomic mass unit (1/12th the mass of a C-12 atom, or 1.66×10^{-27} kg)
UV	ultraviolet
WBG	wide band gap (semiconductor)
w_R	weighting factor for dose equivalence
Z	atomic number (nucleon charge)

References

Aguilar, M., et al. (2010): Relative Composition and Energy Spectra of Light Nuclei in Cosmic Rays: Results From AMS–01. Astrophys. J., vol. 724, no. 1, pp. 329–340.

Akopova, A.B., et al. (2005): Radiation Measurement on the International Space Station. Radiat. Meas., vol. 39, no. 2, pp. 225–228.

Alcaraz, J., et al. (2000a): Leptons in Near Earth Orbit. Phys. Lett. B, vol. 484, pp. 10–22.

Alcaraz, J., et al. (2000b): Protons in Near Earth Orbit. Phys. Lett. B, vol. 472, pp. 215–226.

Bachmair, Felix (2016): Diamond Sensors for Future High Energy Experiments. Nucl. Inst. Meth. Phys. Res. A, vol. 831, pp. 370–377.

Badhwar, G.D. (2001): Radiation Measurements on the International Space Station. Physica Medica, vol. 18, no. 1, pp. 287–291.

Balmain, K.G. (1987): Arc Propagation, Emission and Damage on Spacecraft Dielectrics: A Review. J. Electrostat., vol. 20, no. 1, pp. 95–108.

Beer, J.; Vonmoos, M.; and Muscheler, R. (2006): Solar Variability Over the Past Several Millennia. Space Sci. Rev., vol. 125, pp. 67–79.

Bermudez, V.M. (2005): Theoretical Study of the Electronic Structure of the Si_3N_4(0 0 0 1) Surface. Surf. Sci., vol. 579, pp. 11–20.

Boland, James F. (1970): Nuclear Reactor Instrumentation (In-Core). American Nuclear Society, Lagrange Park, IL.

Boger, J., et al. (2000): The Sudbury Neutrino Observatory. Nuc. Inst. Meth. Phys. Res. A, vol. 449, nos. 1–2, pp. 172–207.

Bowersox, Paul: Up, Up, and Away (2011): Victor Hess and the Cosmic Ray. ANS Nuclear Café, http://ansnuclearcafe.org/2011/08/17/up-up-and-away-victor-hess-and-the-cosmic-ray/ Accessed Nov. 30, 2018.

Brown, Brian H. (2008): Short-Term Changes in Global Cloud Cover and in Cosmic Radiation. J. Atmos. Sol. Terr. Phy., vol. 70, pp. 1122–1131.

Brown, D.A., et al. (2011): Evaluated Nuclear Data File ENDF/B–VIII.0: The 8th Major Release of the Nuclear Reaction Data Library With CIELO-Project Cross Sections, New Standards and Thermal Scattering Data. Nuclear Data Sheets, vol. 112, no. 12, pp. 2887–2996. http://www.nndc.bnl.gov/exfor/endf00.jsp Accessed Feb. 25, 2019.

Budenstein, Paul P. (1980): On the Mechanism of Dielectric Breakdown of Solids. IEEE T. Electr. Insul., vol. EI–15, no. 3, pp. 225–240.

Campins, Humberto; and Krider, E. Philip (1989): Surface Discharges on Natural Dielectrics in the Solar System. Science, vol. 245, no. 4918, pp. 622–624.

Ceramic Industry (2013): Material Properties Charts. Datasheet. BNP Media, Troy, MI. https://www.ceramicindustry.com/ext/resources/pdfs/2013-CCD-Material-Charts.pdf Accessed Feb. 25, 2019.

Chadwick, M.B.; and Normand, E. (1999): Use of New ENDF/B–VI Proton and Neutron Cross Sections for Single Event Upset Calculations. IEEE Trans. Nucl. Sci., vol. 46, no. 6, pp. 1386–1394.

Chen, Liang-Yu, et al. (2013): Packaging Technologies for High Temperature Electronics and Sensors. Proceedings of MFPT 2013/ISA's 29th IIS.

Chronis, Themis G. (2009): Investigating Possible Links Between Incoming Cosmic Ray Fluxes and Lightning Activity Over the United States. J. Clim., vol. 22, pp. 5748–5754.

Clowdsley, M.S., et al. (2005): Radiation on Planetary Surfaces. Solar and Space Physics and the Vision for Space Exploration Meeting, Wintergreen, VA.

Cornélissen, Germaine, et al. (2002): Non-Photic Solar Associations of Heart Rate Variability and Myocardial Infarction. J. Atmos. Sol.-Terr. Phy., vol. 64, nos. 5–6, pp. 707–720.

De Angelis, Alessandro (2013): Spontaneous Ionization to Subatomic Physics: Victor Hess to Peter Higgs. Nuclear Physics B—Proceedings Supplements, vols. 243–244, pp. 3–11.

Dimitrova, S. (2006): Relationship Between Human Physiological Parameters and Geomagnetic Variations of Solar Origin. Adv. Space Res., vol. 37, pp. 1251–1257.

Dorman, L.I., et al. (2003): Thunderstorms' Atmospheric Electric Field Effects in the Intensity of Cosmic Ray Muons and in Neutron Monitor Data. J. Geophys. Res., vol. 108, no. A5, p. 1181.

Frederickson, A.R.; Cotts, D.B.; and Wall, J.A. (1986): Spacecraft Dielectric Material Properties and Spacecraft Charging. American Institute of Aeronautics and Astronautics, Reston, VA.

Friedberg, Wallace; and Copeland, Kyle (2003): What Aircrews Should Know About Their Occupational Exposure to Ionizing Radiation. https://www.nrc.gov/docs/ML1004/ML100481076.pdf Accessed March 11, 2019.

Garrett, Henry B. (2008): Overview of the Jovian Environment. Presented at the OPFM Instrument Workshop.

Gosling, J.T. (2007): Observations of Magnetic Reconnection in the Turbulent High-Speed Solar Wind. Astrophys. J., vol. 671, no. 1, pp. L73–L76.

Gurevich, A.V.; and Milikh, G.M. (1999): Generation of X-Rays due to Multiple Runaway Breakdown Inside Thunderclouds. Phys. Lett. A, vol. 262, no. 6, pp. 457–463.

Gurevich, A.V.; Zybin, K.P.; and Roussel-Dupre, R.A. (1999): Lightning Initiation by Simultaneous Effect of Runaway Breakdown and Cosmic Ray Showers. Phys. Lett. A, vol. 254, nos. 1–2, pp. 79–87.

Gurevich, Aleksandr V.; and Zybin, Kirill P. (2001): Runaway Breakdown and Electric Discharges in Thunderstorms. Phys.-Uspekhi, vol. 44, no. 11, pp. 110 and 119–1140.

Gurevich, Alexander V.; and Zybin, Kirill P. (2005): Runaway Breakdown and the Mysteries of Lightning. Phys. Today, pp. 37–42.

Harrison, R. Giles; and Stephenson, David B. (2006): Empirical Evidence for a Nonlinear Effect of Galactic Cosmic Rays on Clouds. Proc. R. Soc. A., vol. 462, no. 2068, pp. 1121–1233.

Juhasz, Albert J.; Tew, Roy C.; and Schwarze, Gene E. (1998): Impact of Radiation Hardness and Operating Temperatures of Silicon Carbide Electronics on Space Power System Mass. NASA/TM—1998-208826. http://ntrs.nasa.gov

Kniveton, D.R. (2004): Precipitation, Cloud Cover, and Forbush Decreases in Galactic Cosmic Rays. J. Atmos. Sol.-Terr. Phys., vol. 66, nos. 13–14, pp. 1135–1142.

Kohn, Erhard; and Denisenko, Andrej (2007): Concepts for Diamond Electronics. Thin Solid Films, vol. 515, no. 10, pp. 4333–4339.

Larkin, David J., et al. (1994): Site-Competition Epitaxy for Superior Silicon Carbide Electronics. Appl. Phys. Lett., vol. 65, no. 13, p. 1659.

Lechanoine-Leluc, C. (2005): AMS—A Magnetic Spectrometer on the International Space Station. Presented at the 29th International Cosmic Ray Conference, Pune, India, pp. 101–106.

Low, B.C. (2001): Coronal Mass Ejections, Magnetic Flux Ropes, and Solar Magnetism. J. Geophys. Res., vol. 106, no. A11, pp. 25, 141–25, 163.

Marsh, Nigel; and Svensmark, Henrik (2000): Low Cloud Properties Influenced by Cosmic Rays. Phys. Rev. Lett., vol. 85, p. 5004.

McGarrity, J.M., et al. (1992): Silicon Carbide JFET Radiation Response. IEEE Trans. Nucl. Sci., vol. 39, no. 6, pp. 1974–1981.

Mewaldt, R.A. (1996): Anomalous Cosmic Rays: Principal Source of High Energy Ions in the Radiation Belts. Geophysical Monograph Series, vol. 97, pp. 35–41.

Milikh, Gennady; and Roussel-Dupré, Robert (2010): Runaway Breakdown and Electrical Discharges in Thunderstorms. J. Geophys. Res., vol. 115, no. A00E60.

Miller, Earl K.; Freedman, David J.; and Wallis, Jonathan D. (2002): The Prefrontal Cortex: Categories, Concepts and Cognition. Philos. Trans. R. Soc. Lond. B Biol. Sci., vol. 357, pp. 1123–1136.

MolTech GmbH (2013): World of Crystals Datasheet. Molecular Technology GmbH, Berlin, Germany. http://www.mt-berlin.com/frames_cryst/crystals_frameset1.htm Accessed Feb. 25, 2019.

Moore, C.B., et al. (2001): Energetic Radiation Associated With Lightning Stepped-Leaders. Geophys. Res. Lett., vol. 28, no. 11, pp. 2141–2144.

Morselli, A., et al. (2008): GLAST and the Future of High Energy Gamma-Ray Astrophysics. J. Phys. Conf. Ser., vol. 110, p. 062017.

Mulligan, T., et al. (2008): Heliospheric Transient Structures Associated With Short-Period Variations in the GCR Flux. Proceedings of the 30th International Cosmic Ray Conference, R. Caballero, ed., Universidad Nacional Autónoma de México, Mexico City, Mexico, vol. 1, pp. 359–360.

NASA Office of Life and Microgravity Sciences and Applications (OLMSA) (1998): NASA Strategic Program Plan for Space Radiation Health Research.

NASA Science Mission Directorate (2005): Capability Roadmap Report. Science Instruments and Sensors (Roadmap 12).

National Research Council (2008): Managing Space Radiation Risks in the New Era of Space Exploration. Consensus Study Report.

National Research Council (2012a): Earth Science and Applications From Space: A Midterm Assessment of NASA's Implementation of the Decadal Survey. The National Academies Press, Washington, DC. http://www.nap.edu/catalog.php?record_id=13405 Accessed Feb. 25, 2019.

National Research Council (2012b): NASA Space Technology Roadmaps and Priorities. Consensus Study Report.

Nava, F., et al. (2008): Silicon Carbide and Its Use as a Radiation Detector Material. Meas. Sci. Technol., vol. 19, no. 10, p. 102001.

Neudeck, P.G. (1994): Progress Towards High Temperature, High Power SiC Devices. Inst. Phys. Conf. Ser. 141, pp. 1–6.

Nordlund, Kai, et al. (2015): Primary Radiation Damage in Materials. NEA/NSC/DOC(2015)9.

Olive, K.A., et al. (2014): Review of Particle Physics—Particle Data Group. Chin. Phys. C, vol. 38, p. 090001.

O'Neill, K., et al. (2013): Blue Sensitive Silicon Photomultipliers for Fast Timing Applications. Presented at SPIE Photonics West, San Francisco, CA.

Osman, K.T., et al. (2012): Intermittency and Local Heating in the Solar Wind. Phys. Rev. Lett., vol. 108, p. 261102.

Owens, M.J., et al. (2014): Modulation of UK Lightning by Heliospheric Magnetic Field Polarity. Environ. Res. Lett., vol. 9, p. 115009.

Pallé, E.; Butler, C.J.; and O'Brien, K. (2004): The Possible Connection Between Ionization in the Atmosphere by Cosmic Rays and Low Level Clouds. J. Atmos. Sol.-Terr. Phys., vol. 66, pp. 1179–1790.

Paranicas, C., et al. (2009): Europa's Radiation Environment and Its Effects on the Surface. Europa's Radiation Environment, pp. 529–544.

Parihar, Vipan K., et al. (2016): Cosmic Radiation Exposure and Persistent Cognitive Dysfunction. Scientific Reports, vol. 6, p. 34774.

Patterson, Richard, et al. (2013): Impact of Total Ionizing Dose Radiation Testing and Long-Term Thermal Cycling on the Operation of CMF20120D Silicon Carbide Power MOSFET. NASA Electronic Parts and Packaging Program.

Perry, Charles A. (2007): Evidence for a Physical Linkage Between Galactic Cosmic Rays and Regional Climate Time Series. J. Adv. Space Res., vol. 40, no. 3, pp. 353–364.

Petersen, E.L. (1980): Nuclear Reactions in Semiconductors. IEEE Trans. Nucl. Sci., vol. NS–27, no. 6, pp. 1494–1499.

Petersen, E.L. (1992): The Relationship of Proton and Heavy Ion Upset Thresholds. IEEE Trans. Nucl. Sci., vol. 39, no. 6, pp. 1600–1604.

Pudovkin, M.I.; and Veretenenko, S.V. (1995): Cloudiness Decreases Associated With Forbush-Decreases of Galactic Cosmic Rays. J. Atmos. Terr. Phys., vol. 57, no. 11, pp. 1349–1355.

Richardson, John D.; and Wang, Chi (2003): The Solar Wind in the Outer Heliosphere at Solar Maximum. Proceedings of the Tenth International Solar Wind Conference, M. Veili, R. Bruno, and F. Malara, eds., American Institute of Physics CP679, pp. 71–74.

Robertson, J.; and Falabretti, B. (2006): Band Offsets of High K Gate Oxides on III–V Semiconductors. J. Appl. Phys., vol. 100, p. 014111.

Rohs, Susanne, et al. (2010): A Correlation Study of High-Altitude and Midaltitude Clouds and Galactic Cosmic Rays by MIPAS-Envisat. J. Geophys. Res.-Atmos., vol. 115, no. D14.

Ruddy, F.H., et al. (1998): Development of a Silicon Carbide Radiation Detector. IEEE Trans. Nucl. Sci., vol. 45, no. 3, pp. 536–541.

Russell, C.T. (1993): Planetary Magnetospheres. Rep. Prog. Phys., vol. 56, pp. 687–732.

Savani, N.P., et al. (2013): Tracking the Momentum Flux of a CME and Quantifying Its Influence on Geomagnetically Induced Currents at Earth. Space Weather, vol. 11, pp. 245–261.

Scheick, L.; Selva, L.; and Becker, H. (2004): Displacement Damage-Induced Catastrophic Second Breakdown in Silicon Carbide Schottky Power Diodes. IEEE Trans. Nucl. Sci., vol. 51, no. 6, pp. 3193–3200.

Schlegel, K., et al. (2001): Thunderstorms, Lightning and Solar Activity—Middle Europe. J. Atmos. Sol.-Terr. Phys., vol. 63, no. 16, pp. 1705–1713.

Schwadron, N.A., et al. (2010): Earth-Moon-Mars Radiation Environment Module Framework. Space Weather, vol. 8, no. 1.

Scott, C.J., et al. (2014): Evidence for Solar Wind Modulation of Lightning. Environ. Res. Lett., vol. 9, p. 0055004.

Sellin, P.J.; and Vaitkus, J. (2005): New Materials for Radiation Hard Semiconductor Detectors. CERN–OPEN–2005–005.

Siklitski, V., et al. (2001): New Semiconductor Materials. Characteristics and Properties. Ioffe Physico-Technical Institute Electronic Archive. http://www.ioffe.ru/SVA/NSM/Semicond/ Accessed June 8, 2016.

Simonsen, Lisa C. (2000): Background Information for Ionizing Radiation Protection. Presentation by NASA Langley Research Center, Hampton, VA.

Singh, A.K.; Siingh, Devendraa; and Singh, R.P. (2011): Impact of Galactic Cosmic Rays on Earth's Atmosphere and Human Health. Atmos. Environ., vol. 45, no. 23 pp. 3806–3818.

Spence, Harlan E., et al. (2013): Relative Contributions of Galactic Cosmic Rays and Lunar Proton "Albedo" to Dose and Dose Rates Near the Moon. Space Weather, vol. 11, no. 11, pp. 643–650.

Spry, David J., et al. (2016): Prolonged 500 °C Demonstration of 4H-SiC JFET ICs With Two-Level Interconnect. IEEE Electr. Device Lett., vol. 37, no. 5, pp. 625–628.

Stoupel, E. (2006): Cardiac Arrhythmia and Geomagnetic Activity. Indian Pacing Electrophysiol. J., vol. 6, no. 1, pp. 49–53.

Stoupel, E., et al. (2006): Clinical Cosmobiology—Sudden Cardiac Death and Daily/Monthly Geomagnetic, Cosmic Ray and Solar Activity—The Baku Study (2003–2005). Sun Geosph., vol. 1, no. 2, pp. 13–16.

Strong, A.W.; and Moskalenko, I.V. (1998): Propagation of Cosmic-Ray Nucleons in the Galaxy. Astrophys. J., vol. 509, no. 1, pp. 212–228.

Svensmark, J., et al. (2016): The Response of Clouds and Aerosols to Cosmic Ray Decreases. J. Geophys. Res.-Space Phys., vol. 121, no. 9, pp. 8152–8181.

Thompson, Ambler; and Taylor, Barry N. (2008): Guide for the Use of the International System of Units (SI). NIST Special Publication 811.

Tribble, Alan (2010): Energetic Particles and Technology. Heliophysics Space Storms and Radiation: Causes and Effects, Carolus J. Schrijver and George L. Siscoe, eds., Vol. 2, Ch. 14, Cambridge University Press, Cambridge, England pp. 381–400.

Tribble, Alan C. (1993): The Space Environment and Its Impact on Spacecraft Design. AIAA 93–0491.

Tribble, Alan C. (2003): The Space Environment: Implications for Spacecraft Design—Revised and Expanded Edition, Princeton University Press, Princeton, NJ.

Uchihori, Y., et al. (2003): Radiation Measurements Aboard NASA ER–2 High Altitude Aircraft With the Liulin-4J Portable Spectrometer. Adv. Space Res., vol. 32, no. 1 pp. 41–46.

Underwood, C.I. (1998): The Single-Event-Effect Behaviour of Commercial-Off-the-Shelf Memory Devices—A Decade in Low-Earth Orbit. IEEE Trans. Nucl. Sci., vol. 45, no. 3, pp. 1450–1457.

van Lint, V.A.J., et al. (1980): Mechanisms of Radiation Effects in Electronic Materials, Wiley-Interscience, New York, NY.

Vangioni-Flam, Elisabeth; Casse, Michel; and Audouze, Jean (2000): Lithium-Beryllium-Boron: Origin and Evolution. Phys. Rep., vol. 333, pp. 365–387.

Williford, R.E.; Devanathan, R.; and Weber, W.J. (1998): Computer Simulation of Displacement Energies for Several Ceramic Materials. Nucl. Instrum. Methods Phys. Res. B, vol. 141, nos. 1–4, pp. 94–98.

Wilson, J.K., et al. (2013): Cosmic Ray Albedo Proton Yield Correlated With Lunar Elemental Abundances. Presented at the 44th Lunar and Planetary Science Conference, The Woodlands, TX.

Wilson, Jody K., et al. (2012): The First Cosmic Ray Albedo Proton Map of the Moon. J. Geophys. Res.-Planet, vol. 117, no. E00H23.

Wilson, John W., et al. (1997): Galactic and Solar Cosmic Ray Shielding in Deep Space. NASA TP–3682. http://ntrs.nasa.gov

Wing, Simon, et al. (2015): Do Solar Cycles Influence Giant Cell Arteritis and Rheumatoid Arthritis Incidence? BMJ Open, vol. 5, no. 5. https://bmjopen.bmj.com/content/5/5/e006636 Accessed March 5, 2019.

Wrbanek, J.D., et al. (2004): Development of Thin Film Ceramic Thermocouples for High Temperature Environments. AIAA 2004–3549 (NASA/TM—2004-213211). http://ntrs.nasa.gov

Wrbanek, John D., et al. (2007): Micro-Fabricated Solid-State Radiation Detectors for Active Personal Dosimetry. NASA/TM—2007-214674. http://ntrs.nasa.gov

Wrbanek, John D.; Fralick, Gustave C.; and Wrbanek, Susan Y. (2011): Space Radiation Detector With Spherical Geometry. U.S. Patent 7,872,750.

Wrbanek, John D.; Fralick, Gustave C.; and Wrbanek, Susan Y. (2012): Space Radiation Detector With Spherical Geometry. U.S. Patent 8,159,669.

Wrbanek, John D.; Wrbanek, Susan Y.; and Fralick, Gustave C. (2013): Advanced Space Radiation Detector Technology Development. NASA/TM—2013-216516. http://ntrs.nasa.gov

Wrbanek, John D.; and Wrbanek, Susan Y. (2016): Multidirectional Cosmic Ray Ion Detector for Deep Space CubeSats. Proceedings of the AIAA/USU Conference on Small Satellites, Advanced Technologies I, SSC16–IV–2. http://digitalcommons.usu.edu/smallsat/2016/TS4AdvTech1/2/ Accessed March 6, 2019.

Wrbanek, John D.; and Wrbanek, Susan Y. (2018): Fast, Large Area, Wide Band Gap UV Photodetector for Cherenkov Light Detection. U.S. Patent 10,054,691.

Wrbanek, John D.; Wrbanek, Susan Y.; and Fralick, Gustave C. (2013): Advanced Space Radiation Detector Technology Development. NASA/TM—2013-216516. http://ntrs.nasa.gov

Wrbanek, Susan Y.; Wrbanek, John D.; and Fralick, Gustave C. (2019): Low Power Charged Particle Detector. U.S. Patent 10,429,521.

Zhang, T.L., et al. (2007): Little of No Solar Wind Enters Venus' Atmosphere at Solar Minimum. Nature, vol. 450, pp. 654–656.

Ziegler, James F.; Ziegler, M.D.; and Biersack, J.P. (2010): The Stopping and Range of Ions in Matter. Nuclear Instruments and Methods in Physics Research, Sec. B, vol. 268, nos. 11–12, pp. 1818–1823. http://SRIM.org Accessed March 6, 2019.